

Growth patterns for shape-shifting elastic bilayers

Wim M. van Rees^{a,1}, Etienne Vouga^b, and L. Mahadevan^{a,c,d,e,f,2}

^aJohn A. Paulson School of Engineering and Applied Sciences, Harvard University, Cambridge, MA 02138; ^bInstitute for Computational Engineering and Sciences, University of Texas at Austin, Austin, TX 78712; ^cWyss Institute for Biologically Inspired Engineering, Harvard University, Cambridge, MA 02138; ^dDepartment of Physics, Harvard University, Cambridge, MA 02138; ^eDepartment of Organismic and Evolutionary Biology, Harvard University, Cambridge, MA 02138; and ^fKavli Institute for NanoBio Science and Technology, Harvard University, Cambridge, MA 02138

Edited by John A. Rogers, Northwestern University, Evanston, IL, and approved September 6, 2017 (received for review May 31, 2017)

Inspired by the differential-growth-driven morphogenesis of leaves, flowers, and other tissues, there is increasing interest in artificial analogs of these shape-shifting thin sheets made of active materials that respond to environmental stimuli such as heat, light, and humidity. But how can we determine the growth patterns to achieve a given shape from another shape? We solve this geometric inverse problem of determining the growth factors and directions (the metric tensors) for a given isotropic elastic bilayer to grow into a target shape by posing and solving an elastic energy minimization problem. A mathematical equivalence between bilayers and curved monolayers simplifies the inverse problem considerably by providing algebraic expressions for the growth metric tensors in terms of those of the final shape. This approach also allows us to prove that we can grow any target surface from any reference surface using orthotropically growing bilayers. We demonstrate this by numerically simulating the growth of a flat sheet into a face, a cylindrical sheet into a flower, and a flat sheet into a complex canyon-like structure.

inverse physical geometry | growth | form | morphogenesis | 4D printing

Nonuniform in-plane growth of thin sheets generically leads to metric frustration that is relieved by out-of-plane buckling. This mechanism lies at the heart of many morphogenetic processes in botany, such as the shaping of a leaf (1), the blooming of a flower (2), or the explosive dispersal of seeds from certain pods (3). From an engineering perspective, these examples raise the possibility of biomimetic design: programming shape (morphogramming) into matter that can be actuated with environmental signals such as light, temperature, or concentration.

The theory of non-Euclidean plates and shells that links the elastic response of materials into the correctly invariant framework provided by differential geometry (1, 4–8) is a natural starting place to analyze the growth and form of sheets and shells. Growing a thin structure by changing the in-plane intrinsic distances and angles between material elements makes its metric non-Euclidean; generically, this implies that the strain-free reference configuration may not be physically realizable in 3D space. Therefore, the system settles into a residually strained equilibrium configuration that is determined by a local minimum of the energetic cost of stretching and bending the sheet. Generally, this state might not be unique, and, typically, there will be a range of metastable configurations accessible to the system. This raises the natural question of the inverse problem: How should one program growth patterns into a sheet so that it morphs into a prescribed target shape? Recent attempts to solve this question have focused on theoretical designs of optimal growth patterns for the weakly nonlinear deformations of thin shape-shifting isotropic elastic sheets (9), axisymmetric growth patterns for morphable shells (10), design of director fields into deformable nematic elastic sheets (11), or a 4D phytomimetic printing approach based on a linearized elastic analysis to derive the print paths of an anisotropic bilayer made of a responsive ink (12). However, there is no general theoretical or computational framework to solve this inverse problem.

Here, we address this question in the context of a growing elastic bilayer, inspired by the growth and form of plant organs

such as leaves and flowers that are usually made of two cell layers that adhere to each other and can grow independently. This bilayer geometry may be naturally described in terms of an infinitesimally-thin “midsurface” and a “thickness” h that is amenable to a physical description as a thin elastic shell capable of in-plane growth. For very thin plates and shells, an asymptotically correct low-dimensional description of the solid can be used to justify the Kirchhoff–Love assumption, namely, that normals to the cross-section are inextensible and remain normal during deformations. Then, the shell volume is characterized at all times in terms of a solid that extrudes a short distance in the normal direction above and below the midsurface. We assume that growth (i) occurs only in the in-plane directions (tangent to the midsurface) and that (ii) the shell can be divided into several “layers,” with growth constant through the thickness direction for each layer. These assumptions allow us to represent growth within each layer as a tensor field specified at each point of the midsurface. “Isotropic growth” consists of an equal growth factor in all in-plane directions at every point, and is thus encoded by one independent degree of freedom (the isotropic scaling factor) per layer at each point on the midsurface. With “orthotropic growth,” the growth factor of the material at each point is a function of the in-plane direction, providing three degrees of freedom per layer for each location on the midsurface: the two growth factors in the orthogonal “principal growth directions” and the planar rotation angle of this axis. Given the ubiquity of the bilayer geometry in plant organs, and the ease of additive manufacturing techniques that allow us to approach this possibility, we will focus on this case from now on.

Such a bilayer where each of the two layers can experience independent orthotropic growth (Fig. 1, *Left*) has six degrees of

Significance

Many biological forms, such as leaves, flowers, and faces, are shaped by complex growth patterns. How can we prescribe the rules of growth on a simple surface so that it will morph into a flower or a face? Here, we solve this inverse problem of designing the growth patterns for an anisotropically growing elastic bilayer structure and prove that it can be used to achieve any target surface shape from any reference shape. We demonstrate the applicability of this result via the computational design of growth patterns for animal, vegetable, and mineral surfaces—a face, a flower, and a canyon. Our solution provides algorithms for engineering complex functional shapes in tissues, and actuation systems in soft robotics, and elsewhere.

Author contributions: L.M. conceived the study; W.M.v.R., E.V., and L.M. designed research; W.M.v.R. and E.V. performed research; W.M.v.R., E.V., and L.M. analyzed data; and W.M.v.R., E.V., and L.M. wrote the paper.

The authors declare no conflict of interest.

This article is a PNAS Direct Submission.

¹Present address: Department of Mechanical Engineering, Massachusetts Institute of Technology, Cambridge, MA 02139.

²To whom correspondence should be addressed. Email: lmahadev@g.harvard.edu.

This article contains supporting information online at www.pnas.org/lookup/suppl/doi:10.1073/pnas.1709025114/-DCSupplemental.

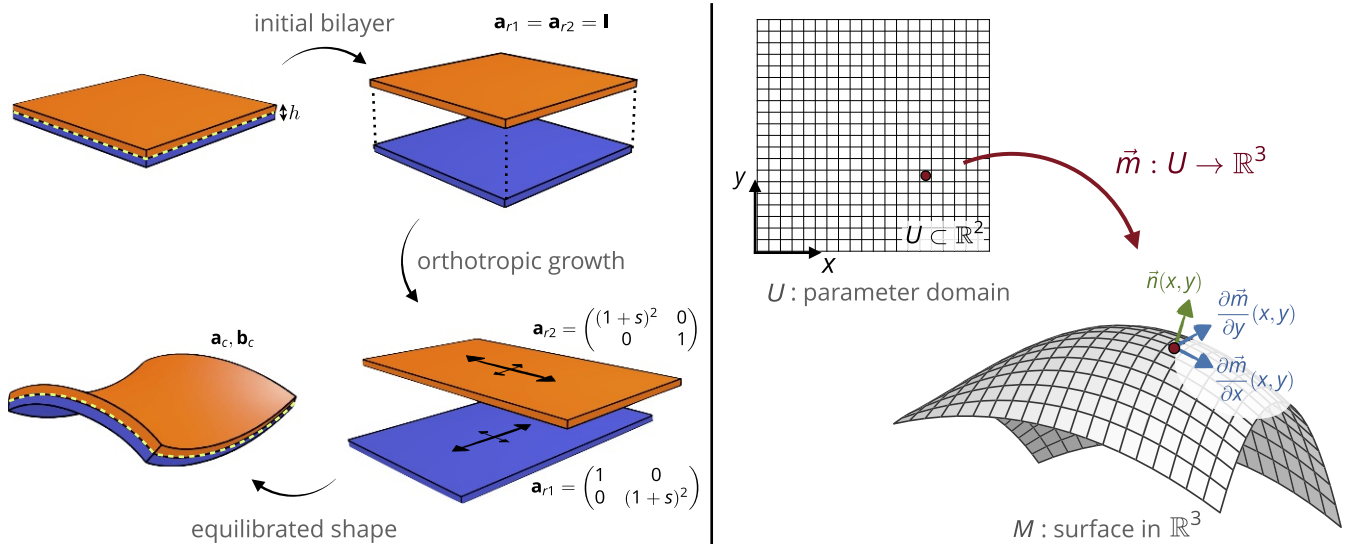


Fig. 1. (Left) A growing bilayer is considered as two independently, possibly inhomogeneously, growing layers, characterized by their own respective metrics \mathbf{a}_{r1} and \mathbf{a}_{r2} , that are glued together at a shared midsurface. In this example, each layer grows in only one direction, orthotropic to that of the other layer, with the linear growth factor $s > 0$. After each layer is grown, the bilayer embedding that minimizes the total elastic energy, characterized by first and second fundamental forms \mathbf{a}_c and \mathbf{b}_c , can be computed. (Right) The surface M is defined as an embedding $\tilde{\mathbf{m}}$ of an arbitrary region of the plane U into \mathbb{R}^3 . The embedding provides a normal field $\tilde{\mathbf{n}}$, as well as the first and second fundamental forms \mathbf{a}_c and \mathbf{b}_c , as described in the text.

freedom at every location along the common midsurface. Any choice of these degrees of freedom constitutes a growth field for the shell, giving rise to an equilibrium shape in \mathbb{R}^3 determined by minimizing the elastic energy of the composite. The design of the growth pattern to achieve a given target shape from an initial reference state leads to the formulation of the following inverse problem: Is it possible to find growth factors and directions for an orthotropically growing bilayer, so that its midsurface changes from a region of the plane or other simple shape initially, into some specified target surface after growth?

Classical differential geometry of 2D surfaces (13) tells us that a surface is uniquely defined by two symmetric quadratic forms (the first and second fundamental form), which consist of six quantities at every location along it. Naive counting of the degrees of freedom suggests that since we have three degrees of freedom associated with the in-plane growth of each of the layers in the composite bilayer, solutions to the inverse problem should be possible. In this work, we show that a solution does indeed always exist for the inverse problem when regularized as an elastic energy minimization problem. Furthermore, while this solution typically does not yield a resultant shape with zero residual strain (due to incompatibility when crossing from one layer to the other through the midsurface), we show that the residual strain is constant (i.e., independent of the realization of the bilayer). We provide a simple algebraic expression for the growth factors and angles that achieve this solution, allowing any bilayer to grow into any target shape.

Geometry and Elasticity

We parameterize the midsurface of a shell using curvilinear coordinates (x, y) in a domain U of the plane, and define its embedding in space by a map $\tilde{\mathbf{m}} : U \rightarrow \mathbb{R}^3$. Each point $\tilde{\mathbf{m}}(x, y)$ on the midsurface is characterized by its tangent vectors $\partial \tilde{\mathbf{m}} / \partial x$ and $\partial \tilde{\mathbf{m}} / \partial y$, and a normal unit vector $\tilde{\mathbf{n}} = (\partial \tilde{\mathbf{m}} / \partial x \times \partial \tilde{\mathbf{m}} / \partial y) / \|\partial \tilde{\mathbf{m}} / \partial x \times \partial \tilde{\mathbf{m}} / \partial y\|$, as shown in Fig. 1, Right. By using the Kirchhoff-Love assumption, any material point \vec{s} inside the volume of the shell can then be written in terms of a normal offset from the midsurface:

$$\vec{s}(x, y, z) = \tilde{\mathbf{m}}(x, y) + z\tilde{\mathbf{n}}(x, y),$$

where $z \in [-h/2, h/2]$, and h is the thickness of the shell. This map gives rise to a metric \mathbf{G} on the volume $U \times [-h/2, h/2]$

$$\mathbf{G}(x, y, z) = (d\vec{s})^T d\vec{s} = \begin{pmatrix} \mathbf{g}_c(x, y, z) & 0 \\ 0 & 1 \end{pmatrix},$$

with the 2×2 tensor \mathbf{g}_c defined as

$$\begin{aligned} \mathbf{g}_c(x, y, z) &\equiv (d\tilde{\mathbf{m}} + z d\tilde{\mathbf{n}})^T (d\tilde{\mathbf{m}} + z d\tilde{\mathbf{n}}) \\ &= \mathbf{a}_c(x, y) - 2z\mathbf{b}_c(x, y) + \mathcal{O}(z^2), \end{aligned}$$

where $\mathbf{a}_c = (d\tilde{\mathbf{m}})^T d\tilde{\mathbf{m}}$ and $\mathbf{b}_c = -(d\tilde{\mathbf{m}})^T d\tilde{\mathbf{n}} = -(d\tilde{\mathbf{n}})^T d\tilde{\mathbf{m}}$ are the first and second fundamental forms of the midsurface in the current configuration. The metric \mathbf{g}_c can be interpreted as measuring the lengths of tangent vectors on any offset surface normal to the midsurface, as well as the angles between them.

Similarly, we can describe the “growth” of U by prescribing a rest (unstrained) metric \mathbf{g}_r to each location in the shell. This rest metric can be written similarly:

$$\mathbf{g}_r(x, y, z) = \mathbf{a}_r(x, y) - 2z\mathbf{b}_r(x, y) + \mathcal{O}(z^2).$$

In general, the shell whose midsurface is described by this growth metric will not have a strain-free embedding in three dimensions, so that for any actual embedding, the shell will be subject to residual strain. To understand which embedding is then realized in physical space, we must therefore turn to a physical description of the shell as an elastic object.

Elastic Energy of a Curved Monolayer. Given the “rest quantities” U , \mathbf{a}_r and \mathbf{b}_r , we can compute for any map $\tilde{\mathbf{m}}$ an elastic potential energy $E(\tilde{\mathbf{m}})$, so that $\tilde{\mathbf{m}}$ is an equilibrium embedding of $(U, \mathbf{a}_r, \mathbf{b}_r)$ whenever $d_{\tilde{\mathbf{m}}} E = 0$ (i.e., whenever $\tilde{\mathbf{m}}$ extremizes the elastic energy). Assuming a hyperelastic isotropic material constitutive model for the material of the shell (known as a St. Venant-Kirchhoff model), we can derive (see SI Appendix for details) the depth-integrated elastic energy as

$$\begin{aligned} E_{ML} = \frac{1}{2} \int_U & \left[\frac{h}{4} \|\mathbf{a}_r^{-1} \mathbf{a}_c - \mathbf{I}\|_e^2 \right. \\ & \left. + \frac{h^3}{12} \|\mathbf{a}_r^{-1} (\mathbf{b}_c - \mathbf{b}_r)\|_e^2 \right] \sqrt{\det \mathbf{a}_r} dx dy, \end{aligned} \quad [1]$$

where \mathbf{a}_c and \mathbf{b}_c are, respectively, the first and second fundamental form of the midsurface in its current realization (and so depend on $\bar{\mathbf{m}}$). Here, the norm $\|\mathbf{A}\|_e^2 = \alpha \text{Tr}^2(\mathbf{A}) + 2\beta \text{Tr}(\mathbf{A}^2)$ defines the elastic constitutive law (14), with $\alpha = Y\nu/(1-\nu^2)$ and $\beta = Y/(2+2\nu)$, where Y is the Young's modulus and ν the Poisson's ratio of the material. We note that this energy formulation contains the classical decomposition into a stretching energy term of $\mathcal{O}(h)$, penalizing the stretch and shear of the midsurface, and a bending energy term of $\mathcal{O}(h^3)$, measuring the resistance to curvature (15). Furthermore, for weakly nonlinear deformations this energy formulation is equivalent to the well-known Föppl–Von Karman formulation for thin elastic plates (see [SI Appendix](#) for details of this equivalence).

Elastic Energy of a Bilayer. A bilayer is made of two monolayers of thickness $h/2$ each, that have been ‘glued’ together at the shared midsurface. Each of the layers has its own independent first fundamental form given by \mathbf{a}_{r1} for the bottom and \mathbf{a}_{r2} for the top layer (Fig. 1, *Left*). Here, ‘bottom’ and ‘top’ are used with the convention of midsurface normal vectors pointing upward (i.e., into the layer whose metric is \mathbf{a}_{r2}).

The elastic energy of a bilayer made of two layers with metrics given by \mathbf{a}_{r1} and \mathbf{a}_{r2} , and a midsurface embedded in \mathbb{R}^3 with first and second fundamental forms \mathbf{a}_c and \mathbf{b}_c , can then be written as the sum of the energies of the individual layers. After integration over the depth of each layer, we obtain the energy as an integral over the common midsurface ([SI Appendix](#))

$$E_{BL} = \frac{1}{2} \int_U \left[\frac{h}{8} \|\mathbf{a}_{r1}^{-1} \mathbf{a}_c - \mathbf{I}\|_e^2 + \frac{h^3}{24} \|\mathbf{a}_{r1}^{-1} \mathbf{b}_c\|_e^2 + \frac{h^2}{8} \langle (\mathbf{a}_{r1}^{-1} \mathbf{a}_c - \mathbf{I}), \mathbf{a}_{r1}^{-1} \mathbf{b}_c \rangle_e \right] \sqrt{\det \mathbf{a}_{r1}} dx dy + \frac{1}{2} \int_U \left[\frac{h}{8} \|\mathbf{a}_{r2}^{-1} \mathbf{a}_c - \mathbf{I}\|_e^2 + \frac{h^3}{24} \|\mathbf{a}_{r2}^{-1} \mathbf{b}_c\|_e^2 - \frac{h^2}{8} \langle (\mathbf{a}_{r2}^{-1} \mathbf{a}_c - \mathbf{I}), \mathbf{a}_{r2}^{-1} \mathbf{b}_c \rangle_e \right] \sqrt{\det \mathbf{a}_{r2}} dx dy, \quad [2]$$

where we have defined an elastic energy inner product $\langle \mathbf{A}, \mathbf{B} \rangle_e = \alpha \text{Tr}(\mathbf{A}) \text{Tr}(\mathbf{B}) + 2\beta \text{Tr}(\mathbf{AB})$. In the special case when the two monolayers grow exactly the same amount starting from a flat reference configuration, $\mathbf{a}_{r1} = \mathbf{a}_{r2} = \mathbf{a}_r$ so that this energy simplifies to the monolayer energy of Eq. 1.

Energy Equivalence Between Monolayers and Bilayers. A natural question that is raised by the geometric and mechanical description of the composite bilayer is whether we can relate it to an equivalent monolayer with appropriate first and second fundamental forms. In this work we show that, indeed, if \mathbf{a}_r and \mathbf{b}_r are appropriately expressed in terms of \mathbf{a}_{r1} and \mathbf{a}_{r2} , the energy of a monolayer can be related to the energy of a bilayer whenever they share the same realization of their midsurfaces.

To see this equivalence, consider the ansatz $\mathbf{a}_r = (\mathbf{a}_{r1} + \mathbf{a}_{r2})/2$ and $\mathbf{b}_r = \zeta(\mathbf{a}_{r1} - \mathbf{a}_{r2})/h$. The simple and natural choice $\zeta = 1/2$ has been proposed in ref. 3 and adopted in ref. 11; however, an analysis of the shell energetics suggests that this value is incorrect: Substituting the ansatz above into the expression for E_{BL} shows that the correct choice is actually $\zeta = 3/4$ as it yields the result (see [SI Appendix](#) for details)

$$E_{BL} = E_{ML} + \int_U \frac{h^3}{72} \|\mathbf{a}_r^{-1} \mathbf{b}_r\|_e^2 \sqrt{\det \mathbf{a}_r} dx dy. \quad [3]$$

The last term on the right side corresponds to a strain that is independent of the embedding, since it does not depend on \mathbf{a}_c and \mathbf{b}_c . This result shows that the minimum-energy realization of a monolayer with reference quadratic forms

$$\mathbf{a}_r = \frac{1}{2}(\mathbf{a}_{r1} + \mathbf{a}_{r2}), \quad \mathbf{b}_r = \frac{3}{4h}(\mathbf{a}_{r1} - \mathbf{a}_{r2}), \quad [4]$$

is identical to that of a bilayer with \mathbf{a}_{r1} and \mathbf{a}_{r2} , allowing for a much simpler representation of the composite made of two elastic layers of the same thickness in terms of an energetically equivalent monolayer with curved reference configuration. The generalization to a bilayer with layers of unequal thicknesses and/or Young's moduli can be solved similarly, where Eqs. 3 and 4 become functions of h_1 , h_2 , Y_1 , and Y_2 , which define the thicknesses and Young's moduli of the bottom and top layer, respectively (see [SI Appendix](#) for details).

Forward Problem of Growth

The result of Eqs. 3 and 4 can be used to compute the quadratic forms \mathbf{a}_r and \mathbf{b}_r , defining the monolayer that is energetically equivalent to a bilayer with individual layer metrics \mathbf{a}_{r1} and \mathbf{a}_{r2} . However, for the corresponding midsurface to have a valid embedding in 3D space, we need to satisfy certain compatibility relations between the first and second fundamental forms. Those relations are given by three differential compatibility relations: the Gauss and Peterson–Mainardi–Codazzi equations (13). The six degrees of freedom of \mathbf{a}_r and \mathbf{b}_r , or equivalently \mathbf{a}_{r1} and \mathbf{a}_{r2} , together with these three differential relations, can be integrated to obtain the three components of $\bar{\mathbf{m}}$ at each location on the surface (up to rigid body motion), as specified by the Bonnet theorem (ref. 16, p. 236); see [SI Appendix](#) for the mathematical details of these constraints.

To give a sense of how this plays out practically, we consider two examples of the forward problem. First, consider the case of Fig. 1, *Left*, where we prescribed orthotropic growth to each of the layers, with the top layer growing in one principal direction and the bottom layer growing in the orthogonal direction. Both layers experience 1D expansion with the same, constant factor s , so that the affected metric entry for each of the layers gets scaled by $(1+s)^2$. The quadratic forms of the energetically equivalent monolayer, \mathbf{a}_r and \mathbf{b}_r , are then given by Eq. 4. It is easy to see that these two forms, being spatially homogeneous, automatically satisfy both of the Peterson–Mainardi–Codazzi equations. Gauss' equation, however, cannot be satisfied: The Gauss curvature K of the suggested embedding is necessarily negative for any growth factor, whereas the derivatives of the metric \mathbf{a}_r are identically zero. This means that no surface with $\mathbf{a}_c = \mathbf{a}_r$ and $\mathbf{b}_c = \mathbf{b}_r$ can exist, as it would violate Gauss's Theorema Egregium (13). The equilibrium configuration in Fig. 1, *Lower Left* is therefore characterized by residual strain (see [SI Appendix](#) for details).

Second, consider a modification of the example of Fig. 1, where the two layers instead grow in the same direction, but with different growth factors s_1 and s_2 . For this case, the first and second fundamental forms \mathbf{a}_r and \mathbf{b}_r satisfy the compatibility relations identically, and correspond to a surface of zero Gauss curvature. Furthermore, if we assume small growth factors, we find that the nonzero principal curvature of the resulting surface is equal to $3/(2h)(s_1 - s_2)$. This result is identical to the classical analysis of Timoshenko (17) for the curvature of heated bimetallic strips, and the correspondence holds also for the case of unequal layer thicknesses and unequal layer Young's moduli (see [SI Appendix](#) for more details). Our solution, summarized in Eqs. 3 and 4, therefore not only generalizes Timoshenko's theory to nonlinear elasticity and arbitrary growth factors, but can also be seen as its extension that allows us to proceed from strips to surfaces.

Inverse Problem of Growth

As noted above, inhomogeneous orthotropic growth for each layer in the bilayer can be represented in terms of three degrees of freedom at every point—two growth factors corresponding to

the growth in orthogonal principal directions and one angle to define the axes. Together, these three values define the symmetric positive definite first fundamental form at a given location. For orthotropic growth of a bilayer, we therefore have independent control of the first fundamental forms for the bottom and top layer, which provides six degrees of freedom for each point on the surface. This leads to the following theorem:

Theorem 1. *Given any surface $M \subset \mathbb{R}^3$ and any shaped planar region $U \subset \mathbb{R}^2$ (topologically compatible with M) with embedding $\tilde{m}: U \rightarrow \mathbb{R}^3$, so that the immersion of \tilde{m} is equal to M , there exists a bilayer $(U, \mathbf{a}_{r1}, \mathbf{a}_{r2})$, with sufficiently small desired thickness h so that \tilde{m} defines the energetically equilibrated configuration of the bilayer's midsurface. This bilayer is defined by*

$$\mathbf{a}_{r1} = \mathbf{a}_c + \frac{2h}{3}\mathbf{b}_c, \quad \mathbf{a}_{r2} = \mathbf{a}_c - \frac{2h}{3}\mathbf{b}_c, \quad [5]$$

where \mathbf{a}_c and \mathbf{b}_c are the first and second fundamental forms of M . Moreover, this embedding is free of residual strain, with the exception of a deformation-independent strain due to incompatibility of the bilayers at their common boundary. Finally, the metrics \mathbf{a}_{r1} and \mathbf{a}_{r2} as defined in Eq. 5 can be decomposed as orthotropic growth of a bilayer on U .

Proof. Eq. 3 states that the minimum energy embedding of a curved monolayer, with $\mathbf{a}_r = (\mathbf{a}_{r1} + \mathbf{a}_{r2})/2$ and $\mathbf{b}_r = 3(\mathbf{a}_{r1} - \mathbf{a}_{r2})/(4h)$, is identical to that of a bilayer with \mathbf{a}_{r1} and \mathbf{a}_{r2} . From Eq. 1 we can immediately see that the minimum energy configuration of a curved monolayer with embedding \tilde{m} is achieved if $\mathbf{a}_r = \mathbf{a}_c$ and $\mathbf{b}_r = \mathbf{b}_c$. With \mathbf{a}_r and \mathbf{b}_r defined as such, we can solve for \mathbf{a}_{r1} and \mathbf{a}_{r2} of the bilayer using Eq. 4, resulting in Eq. 5. From Eq. 3, we can see that the resulting bilayer embedding is free of residual strain except for the already-mentioned deformation-independent term. Finally, by performing a spectral decomposition of the metric, we can write both \mathbf{a}_{r1} and \mathbf{a}_{r2} as orthotropic growth of a bilayer on U . \square

With this theorem, we have the capability to grow any initial bilayer structure into any target shape. However, we need to specify two practical considerations. First of all, the metrics \mathbf{a}_{r1} and \mathbf{a}_{r2} , defined by Eq. 5 have to be positive-definite to be admissible (13). We show in the [SI Appendix](#) that this results in the constraint

$$\max(|\kappa_1|, |\kappa_2|) < \frac{3}{2h},$$

where κ_1 and κ_2 are the principal curvatures of the target surface. In theory, this condition can always be met if the bilayer is thin enough, although in practice, manufacturing constraints on the thickness may limit the space of target shapes that can be grown.

Secondly, the trajectory of growth that is followed to transition from initial to final bilayer metrics might pose complications in practice. Although the embedding of the geometry that globally minimizes the energy given the final bilayer metrics is always unique and identical to the target configuration, some growth trajectories might result in a metastable shape different from the target shape. Since any metastable shape can always be “snapped” into the desired target shape, this issue is of secondary importance to our main contribution, yet provides some interesting questions. In particular, to guarantee that a growth process always results in the target shape, we anticipate two numerical and/or physical difficulties that could arise during interpolation of the metrics. First, it is important for the symmetric positive definite (SPD) matrices encoding the bilayer metrics to vary smoothly over time and remain SPD throughout the interpolation, and, moreover, for the eigenvectors and eigenvalues (encoding the anisotropy amount and direction) to vary as

smoothly as possible during interpolation. Second, interpolated bilayer metrics at intermediate growth stages should remain as compatible as possible; by this, we mean that the first and second fundamental form corresponding to the interpolated bilayer metrics should deviate as little as possible from satisfying the Gauss and Peterson–Mainardi–Codazzi compatibility relations. Otherwise, residual strain accumulates during the interpolation and could pose an energetic barrier between the final realized shape and the target solution. Again, the target solution would still be the global energetic minimum, but physically or numerically, we could find ourselves stuck at a local minimum. A particular numerical example of this is further detailed in the [SI Appendix](#), for the case of the snapdragon flower growth case shown below.

A systematic approach to completely avoiding metastable states during the growth process is a very interesting direction for future work, and we can now pose the problem in a crisp way: Is it possible to interpolate two pairs of bilayer metrics, so that the equivalent minimum-energy midsurface fundamental forms are always compatible? Even more interesting is the prospect to harness incompatibility at intermediate growth stages to control the final grown shape, or exploit multiple solutions depending on the spatiotemporal distribution of growth, for instance, by snap-through (18).

Results

For parametrized surfaces, we can use Eq. 5 directly to solve the inverse problem algebraically. In simple situations associated with parametric surfaces that have explicit fundamental forms (e.g., a hemisphere, catenoid, and a saddle), we can carry out these computations analytically ([SI Appendix](#)). However, to truly demonstrate the usefulness of our approach, we need to show how to design growth patterns for complex shapes with multiple spatial scales. We do this by using numerical methods to minimize Eq. 2. For a given 3D target surface, we first triangulate it using a mesh that can capture the smallest length scale of interest, and then compute the current first and second fundamental forms \mathbf{a}_c and \mathbf{b}_c . We compute the first fundamental forms of the two layers that constitute the bilayer according to Eq. 5, and decompose each of them spectrally into local orthotropic growth rules for a given reference mesh and its corresponding bilayer metrics. We then interpolate the growth factors on each point in the initial mesh into a set of discrete values between those of the reference and target surfaces and solve a sequence of problems to determine the intermediate equilibrium configuration at each of the discrete growth steps. This provides a way to visualize the transition from initial to final configuration in a quasi-static manner, and further allows us to design arbitrary way-points between the initial and final state ([SI Appendix](#)).

Inspired by recent work on floral morphogenesis (19–21), we first show how we can grow a cylinder made of two thin sheets of the same uniform thickness into a snapdragon flower. In this case, we assume the initial cylinder, with \mathbf{a}^{CYL} and \mathbf{b}^{CYL} , is formed by a bilayer with growth factors $\mathbf{a}_{r1}^{\text{CYL}}$ and $\mathbf{a}_{r2}^{\text{CYL}}$, defined according to Eq. 5. The snapdragon flower, with \mathbf{a}^{SD} and \mathbf{b}^{SD} , is similarly represented by a bilayer with $\mathbf{a}_{r1}^{\text{SD}}$ and $\mathbf{a}_{r2}^{\text{SD}}$. To interpolate the reference first fundamental forms of the bilayer from $(\mathbf{a}_{r1}^{\text{CYL}}, \mathbf{a}_{r2}^{\text{CYL}})$ to $(\mathbf{a}_{r1}^{\text{SD}}, \mathbf{a}_{r2}^{\text{SD}})$, we follow a log-Euclidean method (22): Linear interpolation in log-space ensures smoothly varying symmetric positive-definite tensors with monotonically-varying determinants at any point in the growth process. At each intermediate pair of first fundamental forms, we compute the minimum-energy embedding corresponding to the interpolated bilayer metrics. To address the incompatibility of first and second fundamental forms at intermediate stages, we guide the growth process by prescribing four intermediate states, which serve as “way-points” for the growth trajectory (see [SI Appendix](#) for more details). In Fig. 2, *Left*, and [Movie S1](#), we show a sequence of

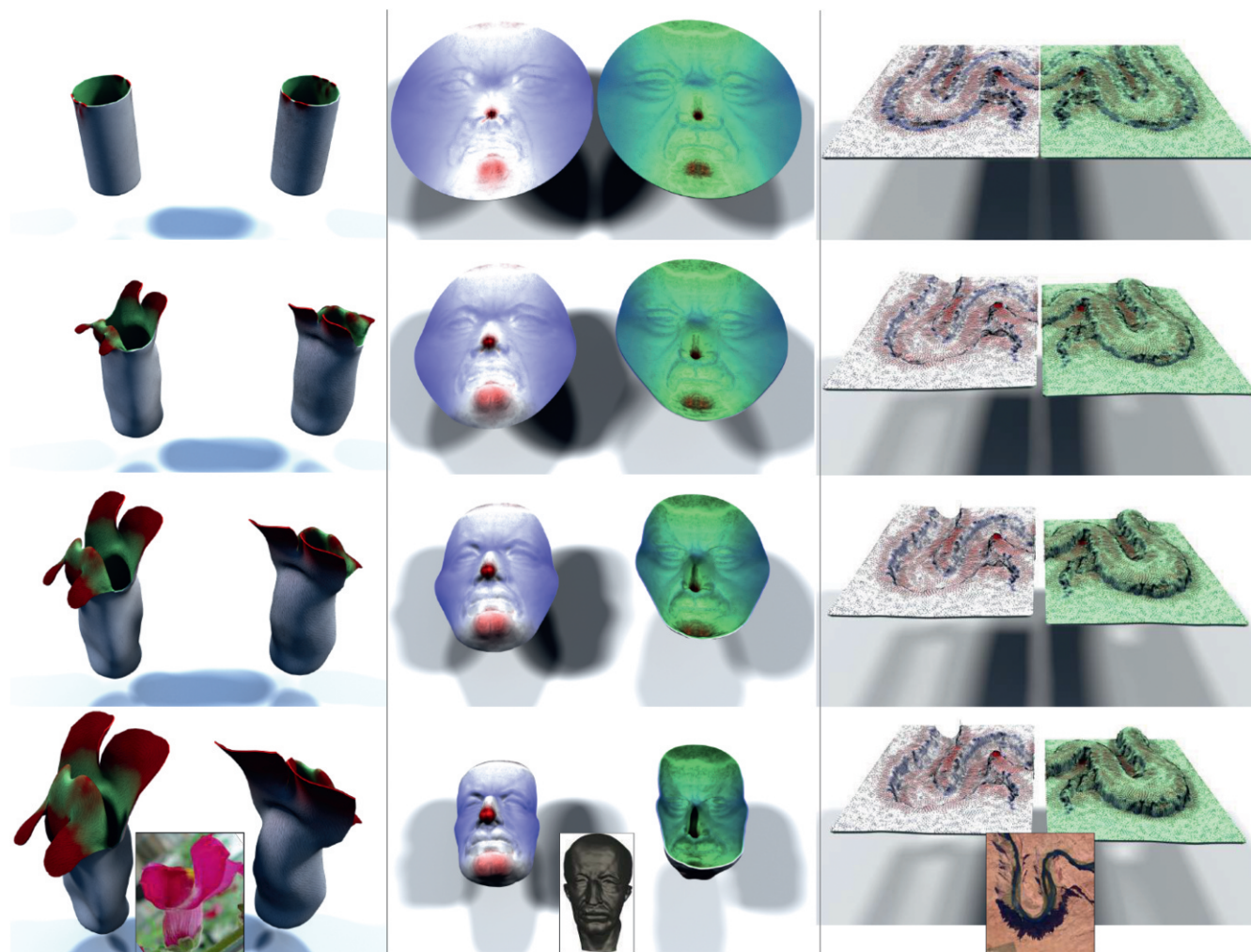


Fig. 2. Inverse design of vegetable, animal, and mineral surfaces. A snapdragon flower petal starting from a cylinder (*Left*), a face starting from a disk (*Center*), and the Colorado River horseshoe bend starting from a rectangle (*Right*). For each example, we show the initial state (top), the final state (bottom) and two intermediate grown states in between. In each state, the colors show the growth factors of the top (left) and bottom (right) layer, and the thin black lines indicate the direction of growth. The top layer is viewed from the front, and the bottom layer is viewed from the back, to highlight the complexity of the geometries. The target shape for each case is given in *Inset* at the bottom: a snapdragon flower (image courtesy of E. Coen); a computer-render of a bust of Max Planck (model is provided courtesy of Max Planck Institute for Informatics by the AIM@SHAPE Shape Repository); a satellite photo of the actual river bend (image courtesy of Google Earth). The height of the actual snapdragon flower is ~ 30 mm (19), whereas the depth of the canyon is 393 m according to USGS elevation data. (See *SI Appendix* for animations and details.)

intermediate shapes viewed from two different angles and, for comparison, the actual snapdragon flower.

To highlight the ability of our approach to capture complex surface geometries with features on multiple scales, we turn to the human face. In Fig. 2, *Center*, and *Movie S2*, we show that we can grow an initially flat bilayer disk into a 3D model of a human face, that of the physicist Max Planck. In this case, we linearly interpolate the growth factors from unity, on the initial disk, to their final values computed from Eq. 5, and show the result for energetic equilibria at two intermediate stages.

Finally, we use our inverse-design theory to grow a simulacrum of a complex inanimate surface, a horseshoe bend in the Colorado River in Arizona. Using United States Geological Survey (USGS) elevation data, we create our 3D target shape and grow it from a rectangular sheet. As in the snapdragon example, we use anchor points to guide the interpolation (see *SI Appendix* for more details). In Fig. 2, *Right*, and *Movie S3*, we show a sequence of intermediate shapes obtained during the growth process. These numerical results demonstrate the practical validity of our theoretical framework that allows us to capture the

shapes of complex absolute-scale-independent surfaces from the animal, vegetable, and mineral world.

Discussion

This study poses and solves the inverse-design problem of designing growth patterns for creating complex shapes from a uniformly thin isotropic elastic bilayer capable of sustaining orthotropic growth. It opens the way for formulating and solving other variants of the inverse-design problem for growth-metric tensors encountered in such cases as a single growing monolayer, isotropically growing bilayers (23), or the most general case of orthotropically growing bilayers with incompatible metrics, all of which will generally require numerical approaches for both the forward and inverse problems. The generalization to account for situations where the thicknesses of the two layers h_1 and h_2 are unequal (*SI Appendix*) provides yet another perspective, as this can be exploited for applications such as artificial lenses (24) or controlled actuation of the curvature in the presence of constraints. It is worth noting that in all of these situations, there are specific instances where the final residually strained state may

constitute an orbit of connected minima associated with a Goldstone mode, e.g., saddle-like solutions in heated or swollen plates (refs. 9 and 15, p. 158), but the general nature of these states and how to design them remains open.

Our approach is agnostic to the actual mechanism that induces this growth, whether it is heat, light, swelling, or biological growth, as long as it is mathematically equivalent to changing the metric of the constituent layers. While the experimental realization of bilayers is easy using additive manufacturing, achieving general orthotropic growth is currently more challenging. An existing technique for orthotropic growth relies on locally embedding fibrils in an isotropically growing base material, providing control over the angle between two fixed orthotropic swelling factors through the print direction (12). To also vary the other two degrees of freedom would require further control over

either the density of the fibrils in two orthogonal directions, or the density in one direction together with the isotropic growth factor of the base material, for each point in each layer. Alternatively, one could consider discrete lattice or origami-type surfaces that approximate the features of a continuous surface at a larger scale. This simplifies the problem by replacing the exact local control of growth by approximate control of an appropriate nonlocal average and is likely to be the first to be realizable experimentally.

ACKNOWLEDGMENTS. We thank E. Coen for the digital surface meshes and image of the snapdragon flower in Fig. 2. This work was supported in part by the Swiss National Science Foundation (to W.M.v.R.), National Science Foundation Grant DMS-1304211 (to E.V.), National Science Foundation Grant DMR 14-20570 (to L.M.), DMREF 15-33985 (to L.M.), and Army Research Office Grant W911NF-15-1-0166 (to L.M.).

- Liang H, Mahadevan L (2009) The shape of a long leaf. *Proc Natl Acad Sci USA* 106:22049–22054.
- Liang H, Mahadevan L (2011) Growth, geometry, and mechanics of a blooming lily. *Proc Natl Acad Sci USA* 108:5516–5521.
- Armon S, Efrati E, Kupferman R, Sharon E (2011) Geometry and mechanics in the opening of chiral seed pods. *Science* 333:1726–1730.
- Ben Amar M, Goriely A (2005) Growth and instability in elastic tissues. *J Mech Phys Solids* 53:2284–2319.
- Klein Y, Efrati E, Sharon E (2007) Shaping of elastic sheets by prescription of non-Euclidean metrics. *Science* 315:1116–1120.
- Dervaux J, Ben Amar M (2008) Morphogenesis of growing soft tissues. *Phys Rev Lett* 101:068101.
- Efrati E, Sharon E, Kupferman R (2009) Elastic theory of unconstrained non-Euclidean plates. *J Mech Phys Solids* 57:762–775.
- Lewicka M, Mahadevan L, Pakzad MR (2011) The Föppl-von Karman equations for plates with incompatible strains. *Proc R Soc A Math Phys Eng Sci* 467:402–426.
- Jones GW, Mahadevan L (2015) Optimal control of plates using incompatible strains. *Nonlinearity* 28:3153–3174.
- Kim J, Hanna JA, Byun M, Santangelo CD, Hayward RC (2012) Designing responsive buckled surfaces by halftone gel lithography. *Science* 335:1201–1205.
- Aharoni H, Sharon E, Kupferman R (2014) Geometry of thin nematic elastomer sheets. *Phys Rev Lett* 113:257801.
- Gladman AS, Matsumoto EA, Nuzzo RG, Mahadevan L, Lewis JA (2016) Biomimetic 4D printing. *Nat Mater* 15:413–418.
- Struik DJ (1988) *Lectures on Classical Differential Geometry* (Dover, New York), 2nd Ed.
- Weischedel C, Tuganov A, Hermansson T, Linn J, Wardetzky M (2012) Construction of discrete shell models by geometric finite differences (Fraunhofer ITWM, Kaiserslautern, Germany), Technical Report 220.
- Mansfield E (1989) *The Bending and Stretching of Plates* (Cambridge Univ Press, Cambridge, UK), 2nd Ed.
- do Carmo MP (1976) *Differential Geometry of Curves and Surfaces* (Prentice-Hall, Englewood Cliffs, NJ).
- Timoshenko S (1925) Analysis of bi-metal thermostats. *J Opt Soc Am* 11:233–255.
- Forterre Y, Skotheim JM, Dumais J, Mahadevan L (2005) How the Venus flytrap snaps. *Nature* 433:421–425.
- Green AA, Kennaway JR, Hanna AI, Bangham JA, Coen E (2010) Genetic control of organ shape and tissue polarity. *PLoS Biol* 8:e1000537.
- Kennaway R, Coen E, Green A, Bangham A (2011) Generation of diverse biological forms through combinatorial interactions between tissue polarity and growth. *PLoS Comput Biol* 7:e1002071.
- Coen E, Rebocho AB (2016) Resolving conflicts: Modeling genetic control of plant morphogenesis. *Dev Cell* 38:579–583.
- Arsigny V, Fillard P, Pennec X, Ayache N (2006) Log-Euclidean metrics for fast and simple calculus on diffusion tensors. *Magn Reson Med* 56:411–421.
- Pezzulla M, Smith GP, Nardinocchi P, Holmes DP (2016) Geometry and mechanics of thin growing bilayers. *Soft Matter* 12:4435–4442.
- Lee LP (2005) Inspirations from biological optics for advanced photonic systems. *Science* 310:1148–1150.

Supplementary Information for “Growth patterns for shape-shifting elastic bilayers”

Contents

S1 Geometry and elasticity	2
S1.1 Elastic energy of a curved monolayer	3
S1.1.1 Energy derivation	4
S1.1.2 Föppl-Von Karman energy for elastic plates	5
S1.2 Elastic energy of a bilayer	7
S1.3 Energy equivalence between mono- and bilayers	8
S1.3.1 Equal layer thicknesses	8
S1.3.2 Unequal layer thicknesses	11
S1.3.3 Unequal layer thicknesses and Young’s moduli	14
S2 Forward problem of growth	16
S2.1 Compatibility relations	16
S2.2 Specialization for isotropically growing bilayer : spherical surfaces	17
S2.3 Specialization for orthogonally growing bilayer : saddle surfaces	18
S2.4 Specialization for parallel growing bilayer : ‘bimetallic strip’	19
S3 Inverse problem of growth	20
S3.1 Constraint on target surface curvature	20
S3.2 Trajectory of growth	21
S4 Results	21
S4.1 Examples for archetypal geometries	22
S4.1.1 Hemisphere	23
S4.1.2 Catenoid	23
S4.1.3 Hyperbolic paraboloid	24
S4.2 Numerical method	24
S4.3 Snapdragon flower	25
S4.4 Max Planck’s face	27
S4.5 Horseshoe bend	28

S1 Geometry and elasticity

This section accompanies the ‘Geometry and elasticity’ section of the main text. Starting with the geometric setting of the problem, we will derive in detail the monolayer energy, the bilayer energy, and the equivalence between the two for equal and unequal layer thicknesses and Young’s moduli.

We parameterize the midsurface of a shell using curvilinear coordinates (x, y) in a domain U of the plane, and define its embedding in space by a map $\vec{m} : U \rightarrow \mathbb{R}^3$. Each point $\vec{m}(x, y)$ on the midsurface is characterized by its tangent vectors $\partial\vec{m}/\partial x$ and $\partial\vec{m}/\partial y$, and a normal unit vector $\vec{n} = (\partial\vec{m}/\partial x \times \partial\vec{m}/\partial y) / \|\partial\vec{m}/\partial x \times \partial\vec{m}/\partial y\|$, as shown in figure 1 of the main text. Using the Kirchhoff-Love assumption, we can extend \vec{m} to an immersion \vec{s} of $U \times [-h/2, h/2]$, where h is the thickness of the shell. This extension dictates that any material point inside the volume of the shell can be written as a normal offset from the midsurface:

$$\vec{s}(x, y, z) = \vec{m}(x, y) + z\vec{n}(x, y),$$

where $z \in [-h/2, h/2]$, and the normal field \vec{n} is defined by

$$\vec{n} = (\partial\vec{m}/\partial x \times \partial\vec{m}/\partial y) / \|\partial\vec{m}/\partial x \times \partial\vec{m}/\partial y\|.$$

This map gives rise to a metric \mathbf{G} on the volume $U \times [-h/2, h/2]$

$$\begin{aligned} \mathbf{G}(x, y, z) &= (d\vec{s})^T d\vec{s} \\ &= \begin{pmatrix} (d\vec{m} + zd\vec{n})^T (d\vec{m} + zd\vec{n}) & 0 \\ 0 & \vec{n}^T \vec{n} \end{pmatrix} \\ &= \begin{pmatrix} \mathbf{g}_c(x, y, z) & 0 \\ 0 & 1 \end{pmatrix}, \end{aligned}$$

where d denotes the differential operator¹. The 2×2 tensor \mathbf{g}_c can be understood as a metric on offset surfaces from the mid-surface. In other words, when extruding a distance z in normal direction from the point (x, y) on the mid-surface, we arrive at an offset surface with metric $\mathbf{g}_c(x, y, z)$. We can expand \mathbf{g}_c as follows

$$\begin{aligned} \mathbf{g}_c(x, y, z) &= (d\vec{m} + zd\vec{n})^T (d\vec{m} + zd\vec{n}) \\ &= (d\vec{m})^T d\vec{m} + z((d\vec{m})^T d\vec{n} + (d\vec{n})^T d\vec{m}) + z^2 (d\vec{n})^T d\vec{n} \\ &= \mathbf{a}_c(x, y) - 2z\mathbf{b}_c(x, y) + z^2\mathbf{c}_c(x, y) \end{aligned}$$

where $\mathbf{a}_c = (d\vec{m})^T d\vec{m}$, $\mathbf{b}_c = -\frac{1}{2}((d\vec{m})^T d\vec{n} + (d\vec{n})^T d\vec{m})$, and $\mathbf{c}_c = (d\vec{n})^T d\vec{n}$, are the first, second and third fundamental forms of the midsurface in the current configuration. It is a standard result that $(d\vec{m})^T d\vec{n}$ is symmetric, so that

$$\mathbf{b}_c = -(d\vec{m})^T d\vec{n} = -(d\vec{n})^T d\vec{m} = \begin{bmatrix} \vec{m}_{xx} \cdot \vec{n} & \vec{m}_{xy} \cdot \vec{n} \\ \vec{m}_{xy} \cdot \vec{n} & \vec{m}_{yy} \cdot \vec{n} \end{bmatrix}$$

Similar to the current configuration, we can define a rest (unstrained) metric \mathbf{g}_r to each location in the shell, which can be written as

$$\mathbf{g}_r(x, y, z) = \mathbf{a}_r(x, y) - 2z\mathbf{b}_r(x, y) + z^2\mathbf{c}_r.$$

¹We use the lower-case d as differential operator, so that if a function $f : \mathbb{R}^n \rightarrow \mathbb{R}^m$, the differential df is a $m \times n$ matrix where the i th column consists of $(\partial f / \partial x_i)$.

As noted in [1], this metric does not need to correspond to any embedding \vec{m}_r of a midsurface in \mathbb{R}^3 , but can rather be abstract (for instance, originating from growth on top of an initially planar structure).

The local, directional Green strain given a point p and vector \vec{w} parallel to the xy plane (by the Kirchhoff-Love assumptions we ignore strain in the thickness direction) is given by

$$\epsilon(p, \vec{w}) = \frac{1}{2} \frac{\vec{w}^T \mathbf{g}_c(p) \vec{w} - \vec{w}^T \mathbf{g}_r \vec{w}}{\vec{w}^T \mathbf{g}_r \vec{w}},$$

and uniformity and isotropy of the shell material implies that the shell energy must be a symmetric function of the eigenvalues of

$$\boldsymbol{\epsilon} = \frac{1}{2} \mathbf{g}_r^{-1} (\mathbf{g}_c - \mathbf{g}_r). \quad (\text{S1.1})$$

Since the elastic energy E is required to be zero and at a local minimum when both eigenvalues are 0, E cannot have any constant term or linear terms in the eigenvalues. A St. Venant-Kirchhoff material model assumes there are no terms higher than quadratic, which leads to an expression for the total energy of the shell,

$$E = \frac{1}{2} \int_U \int_{-h/2}^{h/2} (\alpha \text{Tr}^2(\boldsymbol{\epsilon}) + 2\beta \text{Tr}(\boldsymbol{\epsilon}^2)) \sqrt{\det \mathbf{g}_r} \, dz \, dx \, dy,$$

where α and β are plane-stress Lamé parameters, which can be written in terms of the Young's modulus Y and the Poisson's ratio ν

$$\alpha = \frac{Y\nu}{1-\nu^2}, \quad \beta = \frac{Y}{2(1+\nu)}.$$

We define the elastic energy norm as [2]

$$\|\mathbf{A}\|_e^2 = \alpha \text{Tr}^2(\mathbf{A}) + 2\beta \text{Tr}(\mathbf{A}^2), \quad (\text{S1.2})$$

so the total energy of the shell can be written simply as

$$E = \frac{1}{2} \int_U \int_{-h/2}^{h/2} \|\boldsymbol{\epsilon}\|_e^2 \sqrt{\det \mathbf{g}_r} \, dz \, dx \, dy. \quad (\text{S1.3})$$

S1.1 Elastic energy of a curved monolayer

In this section we will derive the final form of the energy for a thin elastic monolayer, following roughly the derivation of [2]. To simplify notation, we define an elastic energy inner product

$$\langle \mathbf{A}, \mathbf{B} \rangle_e = \alpha \text{Tr}(\mathbf{A}) \text{Tr}(\mathbf{B}) + 2\beta \text{Tr}(\mathbf{AB}),$$

which obeys the following identities

$$\begin{aligned} \langle \mathbf{A}, \mathbf{A} \rangle_e &= \|\mathbf{A}\|_e^2 \\ \langle \lambda \mathbf{A}, \mathbf{B} \rangle_e &= \langle \mathbf{A}, \lambda \mathbf{B} \rangle_e = \lambda \langle \mathbf{A}, \mathbf{B} \rangle_e \\ \langle \mathbf{A}, \mathbf{B} \rangle_e &= \langle \mathbf{B}, \mathbf{A} \rangle_e \\ \langle \mathbf{A} + \mathbf{B}, \mathbf{C} \rangle_e &= \langle \mathbf{A}, \mathbf{C} \rangle_e + \langle \mathbf{B}, \mathbf{C} \rangle_e \end{aligned}$$

S1.1.1 Energy derivation

We can expand \mathbf{g}_r^{-1} as follows:

$$\begin{aligned}\mathbf{g}_r^{-1} &= (\mathbf{a}_r - 2z\mathbf{b}_r + z^2\mathbf{c}_r)^{-1} \\ &= \mathbf{a}_r^{-1} + 2z\mathbf{a}_r^{-1}\mathbf{b}_r\mathbf{a}_r^{-1} + z^2(-\mathbf{a}_r^{-1}\mathbf{c}_r\mathbf{a}_r^{-1} + 4\mathbf{a}_r^{-1}\mathbf{b}_r\mathbf{a}_r^{-1}\mathbf{b}_r\mathbf{a}_r^{-1}) + \mathcal{O}(z^3).\end{aligned}$$

We can therefore write for the strain:

$$\begin{aligned}2\boldsymbol{\epsilon} &= \mathbf{g}_r^{-1}(\mathbf{g}_c - \mathbf{g}_r) = \mathbf{g}_r^{-1}\mathbf{g}_c - \mathbf{I} \\ &= [\mathbf{a}_r^{-1} + 2z\mathbf{a}_r^{-1}\mathbf{b}_r\mathbf{a}_r^{-1} + z^2(-\mathbf{a}_r^{-1}\mathbf{c}_r\mathbf{a}_r^{-1} + 4\mathbf{a}_r^{-1}\mathbf{b}_r\mathbf{a}_r^{-1}\mathbf{b}_r\mathbf{a}_r^{-1}) + \mathcal{O}(z^3)] [\mathbf{a}_c - 2z\mathbf{b}_c + z^2\mathbf{c}_c] - \mathbf{I} \\ &= (\mathbf{a}_r^{-1}\mathbf{a}_c - \mathbf{I}) - (2\mathbf{a}_r^{-1}[\mathbf{b}_c - \mathbf{b}_r\mathbf{a}_r^{-1}\mathbf{a}_c])z + [4\mathbf{a}_r^{-1}\mathbf{b}_r\mathbf{a}_r^{-1}(\mathbf{b}_r\mathbf{a}_r^{-1}\mathbf{a}_c - \mathbf{b}_c) + \mathbf{a}_r^{-1}(\mathbf{c}_c - \mathbf{c}_r\mathbf{a}_r^{-1}\mathbf{a}_c)]z^2 + \mathcal{O}(z^3)\end{aligned}$$

Now we neglect the terms of order $\mathcal{O}(z^2)$ and higher. For the first order term, we further assume that $\|\mathbf{a}_r^{-1}\mathbf{a}_c - \mathbf{I}\|_\infty \leq h$ so that

$$z\mathbf{a}_r^{-1}[\mathbf{b}_c - \mathbf{b}_r\mathbf{a}_r^{-1}\mathbf{a}_c] \approx z\mathbf{a}_r^{-1}(\mathbf{b}_c - \mathbf{b}_r) + \mathcal{O}(h)$$

We then get

$$\boldsymbol{\epsilon} = \frac{1}{2}(\mathbf{a}_r^{-1}\mathbf{a}_c - \mathbf{I}) - z\mathbf{a}_r^{-1}(\mathbf{b}_c - \mathbf{b}_r) + \mathcal{O}(z^2)$$

We can now compute $\|\boldsymbol{\epsilon}\|_e^2$:

$$\begin{aligned}\|\boldsymbol{\epsilon}\|_e^2 &= \langle \boldsymbol{\epsilon}, \boldsymbol{\epsilon} \rangle_e \\ &= \left\langle \frac{1}{2}(\mathbf{a}_r^{-1}\mathbf{a}_c - \mathbf{I}) - z\mathbf{a}_r^{-1}(\mathbf{b}_c - \mathbf{b}_r), \frac{1}{2}(\mathbf{a}_r^{-1}\mathbf{a}_c - \mathbf{I}) - z\mathbf{a}_r^{-1}(\mathbf{b}_c - \mathbf{b}_r) \right\rangle_e \\ &= \frac{1}{4} \|\mathbf{a}_r^{-1}\mathbf{a}_c - \mathbf{I}\|_e^2 + z^2 \|\mathbf{a}_r^{-1}(\mathbf{b}_c - \mathbf{b}_r)\|_e^2 - z \langle (\mathbf{a}_r^{-1}\mathbf{a}_c - \mathbf{I}), \mathbf{a}_r^{-1}(\mathbf{b}_c - \mathbf{b}_r) \rangle_e\end{aligned}$$

The area factor can be expanded as

$$\sqrt{\det \mathbf{g}_r} = \sqrt{\det \mathbf{a}_r} \left(1 - \text{Tr}(\mathbf{a}_r^{-1}\mathbf{b}_r)z + \left(\frac{1}{2} \text{Tr}(\mathbf{a}_r^{-1}\mathbf{c}_r) + \frac{1}{2} \text{Tr}^2(\mathbf{a}_r^{-1}\mathbf{b}_r) - \text{Tr}[(\mathbf{a}_r^{-1}\mathbf{b}_r)^2] \right) z^2 + \mathcal{O}(z^3) \right).$$

Plugging these results into equation (S1.3) and integrating over z , gives the final expression for the monolayer energy

$$\begin{aligned}E_{\text{ML}} &= \frac{1}{2} \int_U \int_{-h/2}^{h/2} \|\boldsymbol{\epsilon}\|_e^2 \sqrt{\det \mathbf{g}_r} \, dz \, dx \, dy \\ &= \frac{1}{2} \int_U \left[\frac{h}{4} \|\mathbf{a}_r^{-1}\mathbf{a}_c - \mathbf{I}\|_e^2 + \frac{h^3}{12} \|\mathbf{a}_r^{-1}(\mathbf{b}_c - \mathbf{b}_r)\|_e^2 \right] \sqrt{\det \mathbf{a}_r} \, dx \, dy + \mathcal{O}(h^4) \\ &= \frac{1}{2} \int_U \mathcal{E}_{\text{ML}} \sqrt{\det \mathbf{a}_r} \, dx \, dy + \mathcal{O}(h^4),\end{aligned}$$

where we have defined the energy density

$$\mathcal{E}_{\text{ML}} = \frac{h}{4} \|\mathbf{a}_r^{-1}\mathbf{a}_c - \mathbf{I}\|_e^2 + \frac{h^3}{12} \|\mathbf{a}_r^{-1}(\mathbf{b}_c - \mathbf{b}_r)\|_e^2.$$

S1.1.2 Föppl-Von Karman energy for elastic plates

To put the energy formulation used in this work into context, here we derive from it the more familiar Föppl-Von Karman energy for the case of a deformed elastic plate.

To define a point on the plate, we use the Cartesian coordinate system on the plane (x, y) to express the midsurface, and define the rest configuration by

$$\vec{m}_r(x, y) = (x, y, 0).$$

We deform the rest configuration according to a displacement field (u, v, w) , leading to the following deformed configuration

$$\vec{m}_c(x, y) = (x + u(x, y), y + v(x, y), w(x, y))$$

For this case, discarding all terms of higher order than quadratic in the deflection, we can write down the Föppl-Von Karman energy as [3, p. 201]

$$\begin{aligned} E_{\text{FVK}} = & \frac{Eh}{2(1-\nu^2)} \iint \left[(\varepsilon_{11} + \varepsilon_{22})^2 - 2(1-\nu) (\varepsilon_{11}\varepsilon_{22} - \varepsilon_{12}^2) \right] dx dy \\ & + \frac{Eh^3}{24(1-\nu^2)} \iint \left[\left(\frac{\partial^2 w}{\partial x^2} + \frac{\partial^2 w}{\partial y^2} \right)^2 - 2(1-\nu) \left(\frac{\partial^2 w}{\partial x^2} \frac{\partial^2 w}{\partial y^2} - \left(\frac{\partial^2 w}{\partial x \partial y} \right)^2 \right) \right] dx dy \end{aligned}$$

where

$$\begin{aligned} \varepsilon_{11} &= \frac{\partial u}{\partial x} + \frac{1}{2} \left(\frac{\partial w}{\partial x} \right)^2 \\ \varepsilon_{12} &= \frac{1}{2} \left(\frac{\partial u}{\partial y} + \frac{\partial v}{\partial x} \right) + \frac{1}{2} \frac{\partial w}{\partial x} \frac{\partial w}{\partial y} \\ \varepsilon_{22} &= \frac{\partial v}{\partial y} + \frac{1}{2} \left(\frac{\partial w}{\partial y} \right)^2. \end{aligned}$$

Here we start with our energy formulation

$$E_{\text{ML}} = \frac{1}{2} \int_U \left[\frac{h}{4} \|\mathbf{a}_r^{-1} \mathbf{a}_c - \mathbf{I}\|_e^2 + \frac{h^3}{12} \|\mathbf{a}_r^{-1} (\mathbf{b}_c - \mathbf{b}_r)\|_e^2 \right] \sqrt{\det \mathbf{a}_r} dx dy,$$

and note immediately that for this particular rest configuration we can compute $\mathbf{a}_r = \mathbf{I}$ and $\mathbf{b}_r = 0$.

For the deformed configuration, we find the coefficients of the first fundamental form \mathbf{a}_c as

$$\begin{aligned} (\mathbf{a}_c)_{11} &= \frac{\partial \vec{m}_c}{\partial x} \cdot \frac{\partial \vec{m}_c}{\partial x} = \left(1 + \frac{\partial u}{\partial x} \right)^2 + \left(\frac{\partial v}{\partial x} \right)^2 + \left(\frac{\partial w}{\partial x} \right)^2 \\ (\mathbf{a}_c)_{12} &= \frac{\partial \vec{m}_c}{\partial x} \cdot \frac{\partial \vec{m}_c}{\partial y} = \left(1 + \frac{\partial u}{\partial x} \right) \frac{\partial u}{\partial y} + \frac{\partial v}{\partial x} \left(1 + \frac{\partial v}{\partial y} \right) + \frac{\partial w}{\partial x} \frac{\partial w}{\partial y} \\ (\mathbf{a}_c)_{22} &= \frac{\partial \vec{m}_c}{\partial y} \cdot \frac{\partial \vec{m}_c}{\partial y} = \left(\frac{\partial u}{\partial y} \right)^2 + \left(1 + \frac{\partial v}{\partial y} \right)^2 + \left(\frac{\partial w}{\partial y} \right)^2, \end{aligned}$$

Applying the assumptions of the Föppl-Von Karman approach, we can simplify this to

$$\begin{aligned}(\mathbf{a}_c)_{11} &= 1 + 2\frac{\partial u}{\partial x} + \left(\frac{\partial w}{\partial x}\right)^2 = 1 + 2\varepsilon_{11} \\(\mathbf{a}_c)_{12} &= \frac{\partial u}{\partial y} + \frac{\partial v}{\partial x} + \frac{\partial w}{\partial x} \frac{\partial w}{\partial y} = 2\varepsilon_{12} \\(\mathbf{a}_c)_{22} &= 1 + 2\frac{\partial v}{\partial y} + \left(\frac{\partial w}{\partial y}\right)^2 = 1 + 2\varepsilon_{22}.\end{aligned}$$

We can use the immersion \vec{m}_c to define the normal vector field as

$$\vec{n}(x, y) = \left(\frac{\partial \vec{m}_c}{\partial x} \times \frac{\partial \vec{m}_c}{\partial y} \right) / \left\| \frac{\partial \vec{m}_c}{\partial x} \times \frac{\partial \vec{m}_c}{\partial y} \right\|$$

For the second fundamental form coefficients, the energy density is multiplied by $\mathcal{O}(h^3)$, and so we the highest order terms:

$$\begin{aligned}(\mathbf{b}_c)_{11} &= -\frac{\partial^2 \vec{m}_c}{\partial x^2} \cdot \vec{n} = -\frac{\partial^2 w}{\partial x^2} \\(\mathbf{b}_c)_{12} &= -\frac{\partial^2 \vec{m}_c}{\partial x \partial y} \cdot \vec{n} = -\frac{\partial^2 w}{\partial x \partial y} \\(\mathbf{b}_c)_{22} &= -\frac{\partial^2 \vec{m}_c}{\partial y^2} \cdot \vec{n} = -\frac{\partial^2 w}{\partial y^2}\end{aligned}$$

Now we can compute the stretching and bending contributions according to the given energy formulation. For the stretching contribution we have

$$\begin{aligned}\|\mathbf{a}_r^{-1} \mathbf{a}_c - \mathbf{I}\|_e^2 &= \|\mathbf{a}_c - \mathbf{I}\|_e^2 = \left\| 2 \begin{pmatrix} \varepsilon_{11} & \varepsilon_{12} \\ \varepsilon_{12} & \varepsilon_{22} \end{pmatrix} \right\|_e^2 \\&= 4 \left[\frac{E\nu}{1-\nu^2} (\varepsilon_{11} + \varepsilon_{22})^2 + \frac{E}{1+\nu} (\varepsilon_{11}^2 + 2\varepsilon_{12}^2 + \varepsilon_{22}^2) \right] \\&= \frac{4E}{1-\nu^2} \left[(\varepsilon_{11} + \varepsilon_{22})^2 - 2(1-\nu) (\varepsilon_{11}\varepsilon_{22} - \varepsilon_{12}^2) \right]\end{aligned}$$

For the bending contribution, we obtain

$$\begin{aligned}\|\mathbf{a}_r^{-1} \mathbf{b}_c\|_e^2 &= \|\mathbf{b}_c\|_e^2 = \left\| - \begin{pmatrix} \partial^2 w / \partial x^2 & \partial^2 w / (\partial x \partial y) \\ \partial^2 w / (\partial x \partial y) & \partial^2 w / \partial y^2 \end{pmatrix} \right\|_e^2 \\&= \frac{E\nu}{1-\nu^2} \left(\frac{\partial^2 w}{\partial x^2} + \frac{\partial^2 w}{\partial y^2} \right)^2 + \frac{E}{1+\nu} \left(\left(\frac{\partial^2 w}{\partial x^2} \right)^2 + 2 \left(\frac{\partial^2 w}{\partial x \partial y} \right)^2 + \left(\frac{\partial^2 w}{\partial y^2} \right)^2 \right) \\&= \frac{E}{1-\nu^2} \left[\left(\frac{\partial^2 w}{\partial x^2} + \frac{\partial^2 w}{\partial y^2} \right)^2 - 2(1-\nu) \left(\frac{\partial^2 w}{\partial x^2} \frac{\partial^2 w}{\partial y^2} - \left(\frac{\partial^2 w}{\partial x \partial y} \right)^2 \right) \right]\end{aligned}$$

Now we can write down the full energy

$$\begin{aligned}E_{\text{ML}} &= \frac{1}{2} \int_U \left[\frac{h}{4} \|\mathbf{a}_r^{-1} \mathbf{a}_c - \mathbf{I}\|_e^2 + \frac{h^3}{12} \|\mathbf{a}_r^{-1} (\mathbf{b}_c - \mathbf{b}_r)\|_e^2 \right] \sqrt{\det \mathbf{a}_r} \, dx \, dy \\&= \frac{Eh}{2(1-\nu^2)} \int_U \left[(\varepsilon_{11} + \varepsilon_{22})^2 - 2(1-\nu) (\varepsilon_{11}\varepsilon_{22} - \varepsilon_{12}^2) \right] \, dx \, dy \\&\quad + \frac{Eh^3}{24(1-\nu^2)} \int_U \left[\left(\frac{\partial^2 w}{\partial x^2} + \frac{\partial^2 w}{\partial y^2} \right)^2 - 2(1-\nu) \left(\frac{\partial^2 w}{\partial x^2} \frac{\partial^2 w}{\partial y^2} - \left(\frac{\partial^2 w}{\partial x \partial y} \right)^2 \right) \right] \, dx \, dy,\end{aligned}$$

which is identical to the FvK energy.

In case we grow the plate, our strain field gets corrected through a multiplicative decomposition of the strain tensor. Applying orthotropic growth to the initial reference metric \mathbf{I} , we assume every material line has grown by a factor s_1 along the direction given by an angle θ with respect to the x coordinate, and by a factor s_2 in the orthogonal direction. We can then write the final, grown metric \mathbf{a}_r through its spectral decomposition as

$$\begin{aligned}\mathbf{a}_r &= \mathbf{R}^T \mathbf{\Lambda} \mathbf{R} \equiv \begin{pmatrix} \cos \theta & \sin \theta \\ -\sin \theta & \cos \theta \end{pmatrix}^T \begin{pmatrix} (1+s_1)^2 & 0 \\ 0 & (1+s_2)^2 \end{pmatrix} \begin{pmatrix} \cos \theta & \sin \theta \\ -\sin \theta & \cos \theta \end{pmatrix} \\ &\approx \begin{pmatrix} \cos \theta & \sin \theta \\ -\sin \theta & \cos \theta \end{pmatrix}^T \begin{pmatrix} 1+2s_1 & 0 \\ 0 & 1+2s_2 \end{pmatrix} \begin{pmatrix} \cos \theta & \sin \theta \\ -\sin \theta & \cos \theta \end{pmatrix} \\ &= \mathbf{I} + 2\mathbf{R}^T \begin{pmatrix} s_1 & 0 \\ 0 & s_2 \end{pmatrix} \mathbf{R} \\ &\equiv \mathbf{I} + 2\boldsymbol{\varepsilon}_g,\end{aligned}$$

where the second step follows from a linearization for small growth factors, and in the last step we introduced the definition of the growth strain $\boldsymbol{\varepsilon}_g$.

Taking the inverse, we can write

$$\mathbf{a}_r^{-1} = (\mathbf{I} + 2\boldsymbol{\varepsilon}_g)^{-1} \approx \mathbf{I} - 2\boldsymbol{\varepsilon}_g,$$

where we used $\|\boldsymbol{\varepsilon}_g\| < 1$. The stretching contribution to the energy then becomes

$$\begin{aligned}\|\mathbf{a}_r^{-1} \mathbf{a}_c - \mathbf{I}\|_e^2 &\approx \|(\mathbf{I} - 2\boldsymbol{\varepsilon}_g) \mathbf{a}_c - \mathbf{I}\|_e^2 \\ &= \|(\mathbf{I} - 2\boldsymbol{\varepsilon}_g)(2\boldsymbol{\varepsilon} + \mathbf{I}) - \mathbf{I}\|_e^2 \\ &\approx \|2(\boldsymbol{\varepsilon} - \boldsymbol{\varepsilon}_g)\|_e^2\end{aligned}$$

where the last step follows if both the strains, and the relative growth factors are small. Furthermore, the correction from the \mathbf{a}_r^{-1} term in the bending strain can be neglected using the same reasoning. This shows how the multiplicative decomposition for growth simplifies to an additive strain contribution after linearization, as exploited by, for instance, [4]. A substantially more in-depth treatment of these different approaches is presented in [5, 6].

S1.2 Elastic energy of a bilayer

The bilayer is formed by two layers of constant thickness $h/2$ each, which share the same midsurface located at $z = 0$. The top layer is the part of the bilayer for which $z > 0$, so that the midsurface normals point into this layer, and the bottom layer is at $z < 0$. Each layer is prescribed its own, independent metric that is constant throughout its respective thickness, denoted as $\mathbf{g}_{r1} = \mathbf{a}_{r1}$ for the bottom, and $\mathbf{g}_{r2} = \mathbf{a}_{r2}$ for the top layer. Any immersion of the bilayer in \mathbb{R}^3 can be described by the immersion of the midsurface, defined by \vec{m} , and giving rise to a first fundamental form \mathbf{a}_c , and a second fundamental form \mathbf{b}_c , similar to the monolayer.

To derive the elastic energy of the bilayer, we start from equation (S1.3) and specialize it for the bilayer case by splitting the integral over the thickness into two components, one

corresponding to each layer:

$$\begin{aligned}
E_{\text{BL}} &= \frac{1}{2} \int_U \int_{-h/2}^0 \|\epsilon_1\|_e^2 \sqrt{\det \mathbf{a}_{r1}} \, dz \, dx \, dy + \frac{1}{2} \int_U \int_0^{h/2} \|\epsilon_2\|_e^2 \sqrt{\det \mathbf{a}_{r2}} \, dz \, dx \, dy \quad (\text{S1.4}) \\
&= \frac{1}{2} \int_U \int_{-h/2}^0 \left[\frac{1}{4} \|\mathbf{a}_{r1}^{-1} \mathbf{a}_c - \mathbf{I}\|_e^2 + z^2 \|\mathbf{a}_{r1}^{-1} \mathbf{b}_c\|_e^2 - z \langle (\mathbf{a}_{r1}^{-1} \mathbf{a}_c - \mathbf{I}), \mathbf{a}_{r1}^{-1} \mathbf{b}_c \rangle_e \right] \sqrt{\det \mathbf{a}_{r1}} \, dx \, dy \\
&\quad + \frac{1}{2} \int_U \int_0^{h/2} \left[\frac{1}{4} \|\mathbf{a}_{r2}^{-1} \mathbf{a}_c - \mathbf{I}\|_e^2 + z^2 \|\mathbf{a}_{r2}^{-1} \mathbf{b}_c\|_e^2 - z \langle (\mathbf{a}_{r2}^{-1} \mathbf{a}_c - \mathbf{I}), \mathbf{a}_{r2}^{-1} \mathbf{b}_c \rangle_e \right] \sqrt{\det \mathbf{a}_{r2}} \, dx \, dy \\
&= \frac{1}{2} \int_U \left[\frac{h}{8} \|\mathbf{a}_{r1}^{-1} \mathbf{a}_c - \mathbf{I}\|_e^2 + \frac{h^3}{24} \|\mathbf{a}_{r1}^{-1} \mathbf{b}_c\|_e^2 + \frac{h^2}{8} \langle (\mathbf{a}_{r1}^{-1} \mathbf{a}_c - \mathbf{I}), \mathbf{a}_{r1}^{-1} \mathbf{b}_c \rangle_e \right] \sqrt{\det \mathbf{a}_{r1}} \, dx \, dy \\
&\quad + \frac{1}{2} \int_U \left[\frac{h}{8} \|\mathbf{a}_{r2}^{-1} \mathbf{a}_c - \mathbf{I}\|_e^2 + \frac{h^3}{24} \|\mathbf{a}_{r2}^{-1} \mathbf{b}_c\|_e^2 + \frac{h^2}{8} \langle (\mathbf{a}_{r2}^{-1} \mathbf{a}_c - \mathbf{I}), \mathbf{a}_{r2}^{-1} \mathbf{b}_c \rangle_e \right] \sqrt{\det \mathbf{a}_{r2}} \, dx \, dy.
\end{aligned}$$

Note: if $\mathbf{a}_{r1} = \mathbf{a}_{r2}$ we recover the monolayer formulation.

S1.3 Energy equivalence between mono- and bilayers

Here we show the energy equivalence between monolayers and bilayers, first for the case where the two layers have equal thickness, and then for the more general case where the layers have different thicknesses.

S1.3.1 Equal layer thicknesses

As described in the main text, in order to show the energetic equivalence between a curved monolayer and a bilayer, we start by making the ansatz

$$\mathbf{a}_r = (\mathbf{a}_{r1} + \mathbf{a}_{r2})/2 \quad (\text{S1.5})$$

$$\mathbf{b}_r = \zeta(\mathbf{a}_{r1} - \mathbf{a}_{r2})/h. \quad (\text{S1.6})$$

We can rewrite those assumptions as

$$\mathbf{a}_{r1} = \mathbf{a}_r + \frac{h}{2\zeta} \mathbf{b}_r = \mathbf{a}_r + \delta \mathbf{a}_r \quad (\text{S1.7})$$

$$\mathbf{a}_{r2} = \mathbf{a}_r - \frac{h}{2\zeta} \mathbf{b}_r = \mathbf{a}_r - \delta \mathbf{a}_r, \quad (\text{S1.8})$$

where $\delta \mathbf{a}_r = \frac{1}{2}(\mathbf{a}_{r1} - \mathbf{a}_{r2}) = h/(2\zeta) \mathbf{b}_r$.

We proceed by expressing the two determinant factors $\sqrt{\det \mathbf{a}_{r1}}$ and $\sqrt{\det \mathbf{a}_{r2}}$ in terms of \mathbf{a}_r and \mathbf{b}_r . Expanding the determinants in h , we can write up to $\mathcal{O}(h^3)$

$$\sqrt{\det \mathbf{a}_{r1}} = \sqrt{\det \mathbf{a}_r} \left(1 + \frac{h}{4\zeta} \text{Tr} [\mathbf{a}_r^{-1} \mathbf{b}_r] + h^2 \left\{ \frac{1}{32\zeta^2} \text{Tr}^2 [\mathbf{a}_r^{-1} \mathbf{b}_r] - \frac{1}{16\zeta^2} \text{Tr} [(\mathbf{a}_r^{-1} \mathbf{b}_r)^2] \right\} \right),$$

and similar for the other layer. We see that up to first order in h , we can write $\sqrt{\det \mathbf{a}_{r1}} \approx \sqrt{\det \mathbf{a}_{r2}} \approx \sqrt{\det \mathbf{a}_r}$.

Next, we look for an expression for the inverse of the layer metrics. We can write

$$\begin{aligned}
\mathbf{a}_{r1}^{-1} &= (\mathbf{a}_r + \delta \mathbf{a}_r)^{-1} = \mathbf{a}_r^{-1} - \mathbf{a}_r^{-1} (\delta \mathbf{a}_r) \mathbf{a}_r^{-1} + \mathbf{a}_r^{-1} ((\delta \mathbf{a}_r) \mathbf{a}_r^{-1})^2 - \dots \\
\mathbf{a}_{r2}^{-1} &= (\mathbf{a}_r - \delta \mathbf{a}_r)^{-1} = \mathbf{a}_r^{-1} + \mathbf{a}_r^{-1} (\delta \mathbf{a}_r) \mathbf{a}_r^{-1} + \mathbf{a}_r^{-1} ((\delta \mathbf{a}_r) \mathbf{a}_r^{-1})^2 + \dots
\end{aligned}$$

We can show that $\|\pm \delta \mathbf{a}_r(\mathbf{a}_r)^{-1}\| < 1$:

$$\|\delta \mathbf{a}_r(\mathbf{a}_r)^{-1}\| = \|(\mathbf{a}_{r2} - \mathbf{a}_{r1})(\mathbf{a}_{r2} + \mathbf{a}_{r1})^{-1}\| = \frac{2h}{\zeta} \|\mathbf{b}_r(\mathbf{a}_r)^{-1}\| = \frac{2h}{\zeta} \|\mathbf{a}_r^{-1} \mathbf{b}_r\| < 1,$$

where the latter is true because principal curvatures are much smaller than h^{-1} , and $h \ll 1$. We therefore discard terms of $((\delta \mathbf{a}_r) \mathbf{a}_r^{-1})^2$ and higher, we can substitute our ansatz in the expression for E_{BL} . We will proceed by considering each of the terms in the energy density, as identified by its order in h .

First-order term We can plug in the definitions for the bottom layer

$$\begin{aligned} \frac{h}{8} \|\mathbf{a}_{r1}^{-1} \mathbf{a}_c - \mathbf{I}\|_e^2 &= \frac{h}{8} \|(\mathbf{a}_r^{-1} - \mathbf{a}_r^{-1}(\delta \mathbf{a}_r) \mathbf{a}_r^{-1}) \mathbf{a}_c - \mathbf{I}\|_e^2 \\ &= \frac{h}{8} \|\mathbf{a}_r^{-1} \mathbf{a}_c - \mathbf{I}\|_e^2 + \frac{h}{8} \|\mathbf{a}_r^{-1}(\delta \mathbf{a}_r) \mathbf{a}_r^{-1} \mathbf{a}_c\|_e^2 - \frac{h}{4} \langle \mathbf{a}_r^{-1} \mathbf{a}_c - \mathbf{I}, \mathbf{a}_r^{-1}(\delta \mathbf{a}_r) \mathbf{a}_r^{-1} \mathbf{a}_c \rangle_e \\ &= \frac{h}{8} \|\mathbf{a}_r^{-1} \mathbf{a}_c - \mathbf{I}\|_e^2 + \frac{h^3}{32\zeta^2} \|\mathbf{a}_r^{-1} \mathbf{b}_r \mathbf{a}_r^{-1} \mathbf{a}_c\|_e^2 - \frac{h^2}{8\zeta} \langle \mathbf{a}_r^{-1} \mathbf{a}_c - \mathbf{I}, \mathbf{a}_r^{-1} \mathbf{b}_r \mathbf{a}_r^{-1} \mathbf{a}_c \rangle_e \\ &= \frac{h}{8} \|\mathbf{a}_r^{-1} \mathbf{a}_c - \mathbf{I}\|_e^2 + \frac{h^3}{32\zeta^2} \|\mathbf{a}_r^{-1} \mathbf{b}_r\|_e^2 - \frac{h^2}{8\zeta} \langle \mathbf{a}_r^{-1} \mathbf{a}_c - \mathbf{I}, \mathbf{a}_r^{-1} \mathbf{b}_r \rangle_e + \mathcal{O}(h^4), \end{aligned}$$

where we used $\mathbf{a}_r^{-1} \mathbf{a}_c = \mathbf{I} + \mathcal{O}(h)$.

Similarly, for the top layer we have

$$\begin{aligned} \frac{h}{8} \|\mathbf{a}_{r2}^{-1} \mathbf{a}_c - \mathbf{I}\|_e^2 &= \frac{h}{8} \|(\mathbf{a}_r^{-1} + \mathbf{a}_r^{-1}(\delta \mathbf{a}_r) \mathbf{a}_r^{-1}) \mathbf{a}_c - \mathbf{I}\|_e^2 \\ &= \frac{h}{8} \|\mathbf{a}_r^{-1} \mathbf{a}_c - \mathbf{I}\|_e^2 + \frac{h^3}{32\zeta^2} \|\mathbf{a}_r^{-1} \mathbf{b}_r\|_e^2 + \frac{h^2}{8\zeta} \langle \mathbf{a}_r^{-1} \mathbf{a}_c - \mathbf{I}, \mathbf{a}_r^{-1} \mathbf{b}_r \rangle_e + \mathcal{O}(h^4). \end{aligned}$$

Multiplying by the area factors, summing, and discarding terms of $\mathcal{O}(h^4)$ and higher gives

$$\frac{h}{8} \left(\|\mathbf{a}_{r1}^{-1} \mathbf{a}_c - \mathbf{I}\|_e^2 \sqrt{\det \mathbf{a}_{r1}} + \|\mathbf{a}_{r2}^{-1} \mathbf{a}_c - \mathbf{I}\|_e^2 \sqrt{\det \mathbf{a}_{r2}} \right) = \left(\frac{h}{4} \|\mathbf{a}_r^{-1} \mathbf{a}_c - \mathbf{I}\|_e^2 + \frac{h^3}{16\zeta^2} \|\mathbf{a}_r^{-1} \mathbf{b}_r\|_e^2 \right) \sqrt{\det \mathbf{a}_r}$$

Second-order term For the second-order term, we have for the bottom layer

$$\begin{aligned} \frac{h^2}{8} \langle (\mathbf{a}_{r1}^{-1} \mathbf{a}_c - \mathbf{I}), \mathbf{a}_{r1}^{-1} \mathbf{b}_c \rangle_e &= \frac{h^2}{8} \langle (\mathbf{a}_r^{-1} - \mathbf{a}_r^{-1}(\delta \mathbf{a}_r) \mathbf{a}_r^{-1}) \mathbf{a}_c - \mathbf{I}, (\mathbf{a}_r^{-1} - \mathbf{a}_r^{-1}(\delta \mathbf{a}_r) \mathbf{a}_r^{-1}) \mathbf{b}_c \rangle_e \\ &= \frac{h^2}{8} \langle (\mathbf{a}_r^{-1} \mathbf{a}_c - \mathbf{I}), \mathbf{a}_r^{-1} \mathbf{b}_c \rangle_e + \frac{h^2}{8} \langle \mathbf{a}_r^{-1}(\delta \mathbf{a}_r) \mathbf{a}_r^{-1} \mathbf{a}_c, \mathbf{a}_r^{-1}(\delta \mathbf{a}_r) \mathbf{a}_r^{-1} \mathbf{b}_c \rangle_e \\ &\quad - \frac{h^2}{8} \langle (\mathbf{a}_r^{-1} \mathbf{a}_c - \mathbf{I}), \mathbf{a}_r^{-1}(\delta \mathbf{a}_r) \mathbf{a}_r^{-1} \mathbf{b}_c \rangle_e - \frac{h^2}{8} \langle \mathbf{a}_r^{-1}(\delta \mathbf{a}_r) \mathbf{a}_r^{-1} \mathbf{a}_c, \mathbf{a}_r^{-1} \mathbf{b}_c \rangle_e \\ &= \frac{h^2}{8} \langle (\mathbf{a}_r^{-1} \mathbf{a}_c - \mathbf{I}), \mathbf{a}_r^{-1} \mathbf{b}_c \rangle_e + \frac{h^4}{32\zeta^2} \langle \mathbf{a}_r^{-1} \mathbf{b}_r \mathbf{a}_r^{-1} \mathbf{a}_c, \mathbf{a}_r^{-1} \mathbf{b}_r \mathbf{a}_r^{-1} \mathbf{b}_c \rangle_e \\ &\quad - \frac{h^3}{16\zeta} \langle (\mathbf{a}_r^{-1} \mathbf{a}_c - \mathbf{I}), \mathbf{a}_r^{-1} \mathbf{b}_r \mathbf{a}_r^{-1} \mathbf{b}_c \rangle_e - \frac{h^3}{16\zeta} \langle \mathbf{a}_r^{-1} \mathbf{b}_r \mathbf{a}_r^{-1} \mathbf{a}_c, \mathbf{a}_r^{-1} \mathbf{b}_c \rangle_e \\ &= \frac{h^2}{8} \langle (\mathbf{a}_r^{-1} \mathbf{a}_c - \mathbf{I}), \mathbf{a}_r^{-1} \mathbf{b}_c \rangle_e - \frac{h^3}{16\zeta} \langle \mathbf{a}_r^{-1} \mathbf{b}_r, \mathbf{a}_r^{-1} \mathbf{b}_c \rangle_e + \mathcal{O}(h^4) \end{aligned}$$

Similarly, for the top layer:

$$\frac{h^2}{8} \langle (\mathbf{a}_{r2}^{-1} \mathbf{a}_c - \mathbf{I}), \mathbf{a}_{r2}^{-1} \mathbf{b}_c \rangle_e = \frac{h^2}{8} \langle (\mathbf{a}_r^{-1} \mathbf{a}_c - \mathbf{I}), \mathbf{a}_r^{-1} \mathbf{b}_c \rangle_e + \frac{h^3}{16\zeta} \langle \mathbf{a}_r^{-1} \mathbf{b}_r, \mathbf{a}_r^{-1} \mathbf{b}_c \rangle_e + \mathcal{O}(h^4)$$

Multiplying by the area factors, summing, and discarding terms of $\mathcal{O}(h^4)$ and higher gives

$$\frac{h^2}{8} \left(\langle (\mathbf{a}_{r1}^{-1} \mathbf{a}_c - \mathbf{I}), \mathbf{a}_{r1}^{-1} \mathbf{b}_c \rangle_e \sqrt{\det \mathbf{a}_{r1}} - \langle (\mathbf{a}_{r2}^{-1} \mathbf{a}_c - \mathbf{I}), \mathbf{a}_{r2}^{-1} \mathbf{b}_c \rangle_e \sqrt{\det \mathbf{a}_{r2}} \right) = -\frac{h^3}{8\zeta} \langle \mathbf{a}_r^{-1} \mathbf{b}_r, \mathbf{a}_r^{-1} \mathbf{b}_c \rangle_e \sqrt{\det \mathbf{a}_r}$$

Third-order term For the bottom layer we have

$$\begin{aligned} \frac{h^3}{24} \|\mathbf{a}_{r1}^{-1} \mathbf{b}_c\|_e^2 &= \frac{h^3}{24} \|(\mathbf{a}_r^{-1} - \mathbf{a}_r^{-1}(\delta \mathbf{a}_r) \mathbf{a}_r^{-1}) \mathbf{b}_c\|_e^2 \\ &= \frac{h^3}{24} \|\mathbf{a}_r^{-1} \mathbf{b}_c\|_e^2 + \frac{h^3}{24} \|\mathbf{a}_r^{-1}(\delta \mathbf{a}_r) \mathbf{a}_r^{-1} \mathbf{b}_c\|_e^2 - \frac{h^3}{12} \langle \mathbf{a}_r^{-1} \mathbf{b}_c, \mathbf{a}_r^{-1}(\delta \mathbf{a}_r) \mathbf{a}_r^{-1} \mathbf{b}_c \rangle_e \\ &= \frac{h^3}{24} \|\mathbf{a}_r^{-1} \mathbf{b}_c\|_e^2 + \frac{h^5}{96\zeta^2} \|\mathbf{a}_r^{-1} \mathbf{b}_r \mathbf{a}_r^{-1} \mathbf{b}_c\|_e^2 - \frac{h^4}{24\zeta} \langle \mathbf{a}_r^{-1} \mathbf{b}_c, \mathbf{a}_r^{-1} \mathbf{b}_r \mathbf{a}_r^{-1} \mathbf{b}_c \rangle_e \\ &= \frac{h^3}{24} \|\mathbf{a}_r^{-1} \mathbf{b}_c\|_e^2 + \mathcal{O}(h^4) \end{aligned}$$

For the top layer similarly:

$$\frac{h^3}{24} \|\mathbf{a}_{r2}^{-1} \mathbf{b}_c\|_e^2 = \frac{h^3}{24} \|\mathbf{a}_r^{-1} \mathbf{b}_c\|_e^2 + \mathcal{O}(h^4)$$

Multiplying by the area factors, summing, and discarding terms of $\mathcal{O}(h^4)$ and higher gives

$$\frac{h^3}{24} \left(\|\mathbf{a}_{r1}^{-1} \mathbf{b}_c\|_e^2 \sqrt{\det \mathbf{a}_{r1}} + \|\mathbf{a}_{r2}^{-1} \mathbf{b}_c\|_e^2 \sqrt{\det \mathbf{a}_{r2}} \right) = \frac{h^3}{12} \|\mathbf{a}_r^{-1} \mathbf{b}_c\|_e^2 \sqrt{\det \mathbf{a}_r}$$

Combining all terms We can now combine all results for the different terms in equation (S1.4):

$$\begin{aligned} E_{\text{BL}} &= \frac{1}{2} \int_U \int_{-h/2}^0 \|\epsilon_1\|_e^2 \sqrt{\det \mathbf{a}_{r1}} \, dz \, dx \, dy + \frac{1}{2} \int_U \int_0^{h/2} \|\epsilon_2\|_e^2 \sqrt{\det \mathbf{a}_{r2}} \, dz \, dx \, dy \\ &= \frac{1}{2} \int_U \frac{h}{8} \left(\|\mathbf{a}_{r1}^{-1} \mathbf{a}_c - \mathbf{I}\|_e^2 \sqrt{\det \mathbf{a}_{r1}} + \|\mathbf{a}_{r2}^{-1} \mathbf{a}_c - \mathbf{I}\|_e^2 \sqrt{\det \mathbf{a}_{r2}} \right) \, dx \, dy \\ &\quad + \frac{1}{2} \int_U \frac{h^3}{24} \left(\|\mathbf{a}_{r1}^{-1} \mathbf{b}_c\|_e^2 \sqrt{\det \mathbf{a}_{r1}} + \|\mathbf{a}_{r2}^{-1} \mathbf{b}_c\|_e^2 \sqrt{\det \mathbf{a}_{r2}} \right) \, dx \, dy \\ &\quad + \frac{1}{2} \int_U \frac{h^2}{8} \left(\langle (\mathbf{a}_{r1}^{-1} \mathbf{a}_c - \mathbf{I}), \mathbf{a}_{r1}^{-1} \mathbf{b}_c \rangle_e \sqrt{\det \mathbf{a}_{r1}} - \langle (\mathbf{a}_{r2}^{-1} \mathbf{a}_c - \mathbf{I}), \mathbf{a}_{r2}^{-1} \mathbf{b}_c \rangle_e \sqrt{\det \mathbf{a}_{r2}} \right) \, dx \, dy \\ &= \frac{1}{2} \int_U \left(\frac{h}{4} \|\mathbf{a}_r^{-1} \mathbf{a}_c - \mathbf{I}\|_e^2 + \frac{h^3}{16\zeta^2} \|\mathbf{a}_r^{-1} \mathbf{b}_r\|_e^2 + \frac{h^3}{12} \|\mathbf{a}_r^{-1} \mathbf{b}_c\|_e^2 - \frac{h^3}{8\zeta} \langle \mathbf{a}_r^{-1} \mathbf{b}_r, \mathbf{a}_r^{-1} \mathbf{b}_c \rangle_e \right) \sqrt{\det \mathbf{a}_r} \, dx \, dy. \end{aligned}$$

Now we readily see that if we choose $\zeta = 3/4$, this expression can be rewritten as

$$\begin{aligned} E_{\text{BL}} &= \frac{1}{2} \int_U \left(\frac{h}{4} \|\mathbf{a}_r^{-1} \mathbf{a}_c - \mathbf{I}\|_e^2 + \frac{h^3}{12} \left(\frac{4}{3} \|\mathbf{a}_r^{-1} \mathbf{b}_r\|_e^2 + \|\mathbf{a}_r^{-1} \mathbf{b}_c\|_e^2 - 2 \langle \mathbf{a}_r^{-1} \mathbf{b}_r, \mathbf{a}_r^{-1} \mathbf{b}_c \rangle_e \right) \right) \sqrt{\det \mathbf{a}_r} \, dx \, dy \\ &= \frac{1}{2} \int_U \left(\frac{h}{4} \|\mathbf{a}_r^{-1} \mathbf{a}_c - \mathbf{I}\|_e^2 + \frac{h^3}{12} \|\mathbf{a}_r^{-1} (\mathbf{b}_c - \mathbf{b}_r)\|_e^2 + \frac{h^3}{36} \|\mathbf{a}_r^{-1} \mathbf{b}_r\|_e^2 \right) \sqrt{\det \mathbf{a}_r} \, dx \, dy \\ &= E_{\text{ML}} + \int_U \frac{h^3}{72} \|\mathbf{a}_r^{-1} \mathbf{b}_r\|_e^2 \sqrt{\det \mathbf{a}_r} \, dx \, dy. \end{aligned}$$

This completes the proof of the energetic equivalence between a bilayer, defined by layer metrics \mathbf{a}_{r1} and \mathbf{a}_{r2} , and a curved monolayer, defined by midsurface quadratic forms \mathbf{a}_r and \mathbf{b}_r , sharing the same midsurface embedding characterized by \mathbf{a}_c and \mathbf{b}_c , whenever

$$\begin{aligned}\mathbf{a}_r &= \frac{1}{2}(\mathbf{a}_{r1} + \mathbf{a}_{r2}), \\ \mathbf{b}_r &= \frac{3}{4h}(\mathbf{a}_{r1} - \mathbf{a}_{r2}),\end{aligned}\tag{S1.9}$$

up to an energy factor that does not depend on the embedding. Or, inversely,

$$\begin{aligned}\mathbf{a}_{r1} &= \mathbf{a}_r + \frac{2h}{3}\mathbf{b}_r, \\ \mathbf{a}_{r2} &= \mathbf{a}_r - \frac{2h}{3}\mathbf{b}_r.\end{aligned}$$

S1.3.2 Unequal layer thicknesses

We consider a structure whose midsurface is located at $z = 0$, but whose top and bottom surface extents are no longer $-h/2 \leq z \leq h/2$, but rather some other bounds $-h_1/2 \leq z \leq h_2/2$, so that the thickness of the bottom layer is $h_1/2$ and the thickness of the top layer is $h_2/2$. We start with the following expression for the energy

$$E = \frac{1}{2} \int_U \int_{-h_1/2}^{h_2/2} \|\epsilon\|_e^2 \sqrt{\det \mathbf{g}_r} \, dz \, dx \, dy.\tag{S1.10}$$

For a monolayer, we obtain the energy integral

$$\begin{aligned}E_{\text{ML}} &= \frac{1}{2} \int_U \int_{-h_1/2}^{h_2/2} \|\epsilon\|_e^2 \sqrt{\det \mathbf{g}_r} \, dz \, dx \, dy \\ &= \frac{1}{2} \int_U \left[\frac{1}{8}(h_2 + h_1) \|\mathbf{a}_r^{-1} \mathbf{a}_c - \mathbf{I}\|_e^2 + \frac{1}{24}(h_2^3 + h_1^3) \|\mathbf{a}_r^{-1}(\mathbf{b}_c - \mathbf{b}_r)\|_e^2 \right. \\ &\quad \left. - \frac{1}{8}(h_2^2 - h_1^2) \langle (\mathbf{a}_r^{-1} \mathbf{a}_c - \mathbf{I}), \mathbf{a}_r^{-1}(\mathbf{b}_c - \mathbf{b}_r) \rangle_e \right] \sqrt{\det \mathbf{a}_r} \, dx \, dy\end{aligned}$$

For the bilayer energy, instead, we find

$$\begin{aligned}E_{\text{BL}} &= \frac{1}{2} \int_U \int_{-h_1/2}^0 \|\epsilon_1\|_e^2 \sqrt{\det \mathbf{a}_{r1}} \, dz \, dx \, dy + \frac{1}{2} \int_U \int_0^{h_2/2} \|\epsilon_2\|_e^2 \sqrt{\det \mathbf{a}_{r2}} \, dz \, dx \, dy \\ &= \frac{1}{2} \int_U \left[\frac{h_1}{8} \|\mathbf{a}_{r1}^{-1} \mathbf{a}_c - \mathbf{I}\|_e^2 + \frac{h_1^3}{24} \|\mathbf{a}_{r1}^{-1} \mathbf{b}_c\|_e^2 + \frac{h_1^2}{8} \langle (\mathbf{a}_{r1}^{-1} \mathbf{a}_c - \mathbf{I}), \mathbf{a}_{r1}^{-1} \mathbf{b}_c \rangle_e \right] \sqrt{\det \mathbf{a}_{r1}} \, dx \, dy \\ &\quad + \frac{1}{2} \int_U \left[\frac{h_2}{8} \|\mathbf{a}_{r2}^{-1} \mathbf{a}_c - \mathbf{I}\|_e^2 + \frac{h_2^3}{24} \|\mathbf{a}_{r2}^{-1} \mathbf{b}_c\|_e^2 - \frac{h_2^2}{8} \langle (\mathbf{a}_{r2}^{-1} \mathbf{a}_c - \mathbf{I}), \mathbf{a}_{r2}^{-1} \mathbf{b}_c \rangle_e \right] \sqrt{\det \mathbf{a}_{r2}} \, dx \, dy.\end{aligned}$$

To mathematically compare these two expressions, we will proceed in the same manner as above. Our ansatz for the bilayer metrics is that they can be written as

$$\begin{aligned}\mathbf{a}_{r1} &= \mathbf{a}_r + \alpha_1 \mathbf{b}_r \\ \mathbf{a}_{r2} &= \mathbf{a}_r - \alpha_2 \mathbf{b}_r,\end{aligned}$$

so that

$$\begin{aligned}\mathbf{a}_r &= \frac{\alpha_2 \mathbf{a}_{r1} + \alpha_1 \mathbf{a}_{r2}}{\alpha_1 + \alpha_2} \\ \mathbf{b}_r &= \frac{\mathbf{a}_{r1} - \mathbf{a}_{r2}}{\alpha_1 + \alpha_2}.\end{aligned}$$

We know that $\alpha_1 \sim \alpha_2 \sim \mathcal{O}(h_1) \sim \mathcal{O}(h_2)$ and will use that to simplify.

We need to find an expression for the inverse of the layer metrics. As before, we can write

$$\begin{aligned}\mathbf{a}_{r1}^{-1} &= (\mathbf{a}_r + \alpha_1 \mathbf{b}_r)^{-1} = \mathbf{a}_r^{-1} - \alpha_1 \mathbf{a}_r^{-1} \mathbf{b}_r \mathbf{a}_r^{-1} - \dots \\ \mathbf{a}_{r2}^{-1} &= (\mathbf{a}_r - \alpha_2 \mathbf{b}_r)^{-1} = \mathbf{a}_r^{-1} + \alpha_2 \mathbf{a}_r^{-1} \mathbf{b}_r \mathbf{a}_r^{-1} + \dots\end{aligned}$$

We discard terms of $\mathcal{O}(\alpha_1^2, \alpha_2^2)$ and higher, and continue by treating each term in the energy equation separately in the following.

First-order term We can plug in the definitions for the bottom layer

$$\begin{aligned}\frac{h_1}{8} \|\mathbf{a}_{r1}^{-1} \mathbf{a}_c - \mathbf{I}\|_e^2 &= \frac{h_1}{8} \|(\mathbf{a}_r^{-1} - \alpha_1 \mathbf{a}_r^{-1} \mathbf{b}_r \mathbf{a}_r^{-1}) \mathbf{a}_c - \mathbf{I}\|_e^2 \\ &= \frac{h_1}{8} \|\mathbf{a}_r^{-1} \mathbf{a}_c - \mathbf{I}\|_e^2 + \frac{h_1 \alpha_1^2}{8} \|\mathbf{a}_r^{-1} \mathbf{b}_r \mathbf{a}_r^{-1} \mathbf{a}_c\|_e^2 - \frac{h_1}{4} \alpha_1 \langle \mathbf{a}_r^{-1} \mathbf{a}_c - \mathbf{I}, \mathbf{a}_r^{-1} \mathbf{b}_r \mathbf{a}_r^{-1} \mathbf{a}_c \rangle_e \\ &= \frac{h_1}{8} \|\mathbf{a}_r^{-1} \mathbf{a}_c - \mathbf{I}\|_e^2 + \frac{h_1 \alpha_1^2}{8} \|\mathbf{a}_r^{-1} \mathbf{b}_r\|_e^2 - \frac{h_1}{4} \alpha_1 \langle \mathbf{a}_r^{-1} \mathbf{a}_c - \mathbf{I}, \mathbf{a}_r^{-1} \mathbf{b}_r \rangle_e + \mathcal{O}(h^4),\end{aligned}$$

where we used $\mathbf{a}_r^{-1} \mathbf{a}_c = \mathbf{I} + \mathcal{O}(h)$.

Similarly, for the top layer we have

$$\begin{aligned}\frac{h_2}{8} \|\mathbf{a}_{r2}^{-1} \mathbf{a}_c - \mathbf{I}\|_e^2 &= \frac{h_2}{8} \|(\mathbf{a}_r^{-1} + \alpha_2 \mathbf{a}_r^{-1} \mathbf{b}_r \mathbf{a}_r^{-1}) \mathbf{a}_c - \mathbf{I}\|_e^2 \\ &= \frac{h_2}{8} \|\mathbf{a}_r^{-1} \mathbf{a}_c - \mathbf{I}\|_e^2 + \frac{h_2 \alpha_2^2}{8} \|\mathbf{a}_r^{-1} \mathbf{b}_r\|_e^2 + \frac{h_2}{4} \alpha_2 \langle \mathbf{a}_r^{-1} \mathbf{a}_c - \mathbf{I}, \mathbf{a}_r^{-1} \mathbf{b}_r \rangle_e + \mathcal{O}(h^4)\end{aligned}$$

Multiplying by the area factors, summing, and discarding terms of $\mathcal{O}(h^4)$ and higher gives

$$\begin{aligned}\frac{h_1}{8} \|\mathbf{a}_{r1}^{-1} \mathbf{a}_c - \mathbf{I}\|_e^2 \sqrt{\det \mathbf{a}_{r1}} &+ \frac{h_2}{8} \|\mathbf{a}_{r2}^{-1} \mathbf{a}_c - \mathbf{I}\|_e^2 \sqrt{\det \mathbf{a}_{r2}} = \\ &= \left(\frac{h_1 + h_2}{8} \|\mathbf{a}_r^{-1} \mathbf{a}_c - \mathbf{I}\|_e^2 + \frac{h_1 \alpha_1^2 + h_2 \alpha_2^2}{8} \|\mathbf{a}_r^{-1} \mathbf{b}_r\|_e^2 + \frac{h_2 \alpha_2 - h_1 \alpha_1}{4} \langle \mathbf{a}_r^{-1} \mathbf{a}_c - \mathbf{I}, \mathbf{a}_r^{-1} \mathbf{b}_r \rangle_e \right) \sqrt{\det \mathbf{a}_r}\end{aligned}$$

Second-order term For the second term, we have for the bottom layer

$$\begin{aligned}\frac{h_1^2}{8} \langle (\mathbf{a}_{r1}^{-1} \mathbf{a}_c - \mathbf{I}), \mathbf{a}_{r1}^{-1} \mathbf{b}_c \rangle_e &= \frac{h_1^2}{8} \langle (\mathbf{a}_r^{-1} - \alpha_1 \mathbf{a}_r^{-1} \mathbf{b}_r \mathbf{a}_r^{-1}) \mathbf{a}_c - \mathbf{I}, (\mathbf{a}_r^{-1} - \alpha_1 \mathbf{a}_r^{-1} \mathbf{b}_r \mathbf{a}_r^{-1}) \mathbf{b}_c \rangle_e \\ &= \frac{h_1^2}{8} \langle (\mathbf{a}_r^{-1} \mathbf{a}_c - \mathbf{I}), \mathbf{a}_r^{-1} \mathbf{b}_c \rangle_e + \frac{h_1^2 \alpha_1^2}{8} \langle \mathbf{a}_r^{-1} \mathbf{b}_r \mathbf{a}_r^{-1} \mathbf{a}_c, \mathbf{a}_r^{-1} \mathbf{b}_r \mathbf{a}_r^{-1} \mathbf{b}_c \rangle_e \\ &\quad - \frac{h_1^2 \alpha_1}{8} \langle (\mathbf{a}_r^{-1} \mathbf{a}_c - \mathbf{I}), \mathbf{a}_r^{-1} \mathbf{b}_r \mathbf{a}_r^{-1} \mathbf{b}_c \rangle_e - \frac{h_1^2 \alpha_1}{8} \langle \mathbf{a}_r^{-1} \mathbf{b}_r \mathbf{a}_r^{-1} \mathbf{a}_c, \mathbf{a}_r^{-1} \mathbf{b}_c \rangle_e \\ &= \frac{h_1^2}{8} \langle (\mathbf{a}_r^{-1} \mathbf{a}_c - \mathbf{I}), \mathbf{a}_r^{-1} \mathbf{b}_c \rangle_e - \frac{h_1^2 \alpha_1}{8} \langle \mathbf{a}_r^{-1} \mathbf{b}_r \mathbf{a}_r^{-1} \mathbf{a}_c, \mathbf{a}_r^{-1} \mathbf{b}_c \rangle_e + \mathcal{O}(h^4) \\ &= \frac{h_1^2}{8} \langle (\mathbf{a}_r^{-1} \mathbf{a}_c - \mathbf{I}), \mathbf{a}_r^{-1} \mathbf{b}_c \rangle_e - \frac{h_1^2 \alpha_1}{8} \langle \mathbf{a}_r^{-1} \mathbf{b}_r, \mathbf{a}_r^{-1} \mathbf{b}_c \rangle_e + \mathcal{O}(h^4)\end{aligned}$$

Similarly, for the top layer:

$$\frac{h_2^2}{8} \langle (\mathbf{a}_{r2}^{-1} \mathbf{a}_c - \mathbf{I}), \mathbf{a}_{r2}^{-1} \mathbf{b}_c \rangle_e = \frac{h_2^2}{8} \langle (\mathbf{a}_r^{-1} \mathbf{a}_c - \mathbf{I}), \mathbf{a}_r^{-1} \mathbf{b}_c \rangle_e + \frac{h_2^2 \alpha_2}{8} \langle \mathbf{a}_r^{-1} \mathbf{b}_r, \mathbf{a}_r^{-1} \mathbf{b}_c \rangle_e + \mathcal{O}(h^4)$$

Multiplying by the area factors, subtracting the top-layer term from the bottom-layer term, and discarding terms of $\mathcal{O}(h^4)$ and higher gives

$$\begin{aligned} & \frac{h_1^2}{8} \langle (\mathbf{a}_{r1}^{-1} \mathbf{a}_c - \mathbf{I}), \mathbf{a}_{r1}^{-1} \mathbf{b}_c \rangle_e \sqrt{\det \mathbf{a}_{r1}} - \frac{h_2^2}{8} \langle (\mathbf{a}_{r2}^{-1} \mathbf{a}_c - \mathbf{I}), \mathbf{a}_{r2}^{-1} \mathbf{b}_c \rangle_e \sqrt{\det \mathbf{a}_{r2}} = \\ & = \left[\left(\frac{h_1^2 - h_2^2}{8} \right) \langle (\mathbf{a}_r^{-1} \mathbf{a}_c - \mathbf{I}), \mathbf{a}_r^{-1} \mathbf{b}_c \rangle_e - \frac{h_1^2 \alpha_1 + h_2^2 \alpha_2}{8} \langle \mathbf{a}_r^{-1} \mathbf{b}_r, \mathbf{a}_r^{-1} \mathbf{b}_c \rangle_e \right] \sqrt{\det \mathbf{a}_r} \end{aligned}$$

Third-order term For the bottom layer we have

$$\begin{aligned} \frac{h_1^3}{24} \|\mathbf{a}_{r1}^{-1} \mathbf{b}_c\|_e^2 &= \frac{h_1^3}{24} \|(\mathbf{a}_r^{-1} - \alpha_1 \mathbf{a}_r^{-1} \mathbf{b}_r \mathbf{a}_r^{-1}) \mathbf{b}_c\|_e^2 \\ &= \frac{h_1^3}{24} \|\mathbf{a}_r^{-1} \mathbf{b}_c\|_e^2 + \frac{h_1^3 \alpha_1^2}{24} \|\mathbf{a}_r^{-1} \mathbf{b}_r \mathbf{a}_r^{-1} \mathbf{b}_c\|_e^2 - \frac{h_1^3 \alpha_1}{12} \langle \mathbf{a}_r^{-1} \mathbf{b}_c, \mathbf{a}_r^{-1} \mathbf{b}_r \mathbf{a}_r^{-1} \mathbf{b}_c \rangle_e \\ &= \frac{h_1^3}{24} \|\mathbf{a}_r^{-1} \mathbf{b}_c\|_e^2 + \mathcal{O}(h^4) \end{aligned}$$

For the top layer similarly:

$$\frac{h_2^3}{24} \|\mathbf{a}_{r2}^{-1} \mathbf{b}_c\|_e^2 = \frac{h_2^3}{24} \|\mathbf{a}_r^{-1} \mathbf{b}_c\|_e^2 + \mathcal{O}(h^4)$$

Multiplying by the area factors, summing, and discarding terms of $\mathcal{O}(h^4)$ and higher gives

$$\frac{h_1^3}{24} \|\mathbf{a}_{r1}^{-1} \mathbf{b}_c\|_e^2 \sqrt{\det \mathbf{a}_{r1}} + \frac{h_2^3}{24} \|\mathbf{a}_{r2}^{-1} \mathbf{b}_c\|_e^2 \sqrt{\det \mathbf{a}_{r2}} = \frac{h_1^3 + h_2^3}{24} \|\mathbf{a}_r^{-1} \mathbf{b}_c\|_e^2 \sqrt{\det \mathbf{a}_r}$$

Combining all terms Recalling the energy density definition for the unequal-thickness bilayer, we can now plug in the above results:

$$\begin{aligned} \mathcal{E}_{\text{BL}} &= \frac{h_1 + h_2}{8} \|\mathbf{a}_r^{-1} \mathbf{a}_c - \mathbf{I}\|_e^2 + \frac{h_1 \alpha_1^2 + h_2 \alpha_2^2}{8} \|\mathbf{a}_r^{-1} \mathbf{b}_r\|_e^2 + \frac{h_2 \alpha_2 - h_1 \alpha_1}{4} \langle \mathbf{a}_r^{-1} \mathbf{a}_c - \mathbf{I}, \mathbf{a}_r^{-1} \mathbf{b}_r \rangle_e \\ &+ \left(\frac{h_1^2 - h_2^2}{8} \right) \langle (\mathbf{a}_r^{-1} \mathbf{a}_c - \mathbf{I}), \mathbf{a}_r^{-1} \mathbf{b}_c \rangle_e - \frac{h_1^2 \alpha_1 + h_2^2 \alpha_2}{8} \langle \mathbf{a}_r^{-1} \mathbf{b}_r, \mathbf{a}_r^{-1} \mathbf{b}_c \rangle_e + \frac{h_1^3 + h_2^3}{24} \|\mathbf{a}_r^{-1} \mathbf{b}_c\|_e^2 \end{aligned}$$

For reference, the unequal-thickness monolayer energy density is

$$\mathcal{E}_{\text{ML}} = \frac{1}{8} (h_2 + h_1) \|\mathbf{a}_r^{-1} \mathbf{a}_c - \mathbf{I}\|_e^2 + \frac{1}{24} (h_2^3 + h_1^3) \|\mathbf{a}_r^{-1} (\mathbf{b}_c - \mathbf{b}_r)\|_e^2 - \frac{1}{8} (h_2^2 - h_1^2) \langle (\mathbf{a}_r^{-1} \mathbf{a}_c - \mathbf{I}), \mathbf{a}_r^{-1} (\mathbf{b}_c - \mathbf{b}_r) \rangle_e.$$

To equate them, the following equations have to be satisfied:

$$\frac{h_1 \alpha_1^2 + h_2 \alpha_2^2}{8} = \frac{1}{24} (h_2^3 + h_1^3) + c \quad (\text{S1.11})$$

$$\frac{h_2 \alpha_2 - h_1 \alpha_1}{4} = \frac{1}{8} (h_2^2 - h_1^2) \quad (\text{S1.12})$$

$$\frac{h_1^2 \alpha_1 + h_2^2 \alpha_2}{8} = \frac{1}{12} (h_2^3 + h_1^3). \quad (\text{S1.13})$$

Here c represents an additional scalar constant that multiplies $\|\mathbf{a}_r^{-1}\mathbf{b}_r\|_e^2$, and therefore does not change the equilibrium configuration but closes the system of equations. We solve the last two equations for α_2 and α_1 , and then plug the solution into the first to compute c . We then find

$$\begin{aligned}\alpha_1 &= \frac{4h_1^2 - h_1h_2 + h_2^2}{6h_1} \\ \alpha_2 &= \frac{4h_2^2 - h_1h_2 + h_1^2}{6h_2} \\ c &= \frac{(h_1 + h_2)^3(h_2^2 - h_1h_2 + h_1^2)}{288h_1h_2}\end{aligned}$$

Plugging this into our ansatz gives

$$\begin{aligned}\mathbf{a}_{r1} &= \mathbf{a}_r + \left(\frac{4h_1^2 - h_1h_2 + h_2^2}{6h_1}\right)\mathbf{b}_r \\ \mathbf{a}_{r2} &= \mathbf{a}_r - \left(\frac{4h_2^2 - h_1h_2 + h_1^2}{6h_2}\right)\mathbf{b}_r,\end{aligned}$$

and

$$\begin{aligned}\mathbf{a}_r &= \frac{h_1(4h_2^2 - h_1h_2 + h_1^2)}{(h_1 + h_2)^3}\mathbf{a}_{r1} + \frac{h_2(4h_1^2 - h_1h_2 + h_2^2)}{(h_1 + h_2)^3}\mathbf{a}_{r2}, \\ \mathbf{b}_r &= \frac{6h_1h_2}{(h_1 + h_2)^3}(\mathbf{a}_{r1} - \mathbf{a}_{r2}).\end{aligned}\tag{S1.14}$$

With these solutions, the final energy equivalence is

$$E_{\text{BL}} = E_{\text{ML}} + \int_U \frac{c}{2} \|\mathbf{a}_r^{-1}\mathbf{b}_r\|_e^2 \sqrt{\det \mathbf{a}_r} \, dx \, dy.\tag{S1.15}$$

Note: if $h_1 = h_2 = h$, we find $\alpha_1 = \alpha_2 = 2h/3$, and $c = h^3/36$, consistent with the previous derivation.

S1.3.3 Unequal layer thicknesses and Young's moduli

Here we wish to find the monolayer that is energetically equivalent to a bilayer with unequal layer thicknesses as well as unequal layer Young's moduli. Here the usage of the term 'monolayer' might be misleading, since we are actually calculating the first and second fundamental form of a curved mid-surface that is surrounded by the same material as the original bilayer. This means our equivalent 'monolayer' does in fact consist of two layers of different material, each characterized by its own Young's modulus. The technical difference between the original bilayer and the equivalent monolayer, is that the former is characterized in terms its two layer metrics, whereas the latter is characterized by the first and second fundamental form of its midsurface – allowing us to solve the inverse-problem of growth exactly.

Using this perspective, defining the Young's modulus of the bottom and top layer by Y_1 and Y_2 , respectively, we can write the energy of the original bilayer, and the equivalent 'monolayer', as

$$\begin{aligned}E_{\text{BL}} &= \frac{1}{2} \int_U Y_1 \left[\frac{h_1}{8} \|\mathbf{a}_{r1}^{-1}\mathbf{a}_c - \mathbf{I}\|_{e/Y}^2 + \frac{h_1^3}{24} \|\mathbf{a}_{r1}^{-1}\mathbf{b}_c\|_{e/Y}^2 + \frac{h_1^2}{8} \langle (\mathbf{a}_{r1}^{-1}\mathbf{a}_c - \mathbf{I}), \mathbf{a}_{r1}^{-1}\mathbf{b}_c \rangle_{e/Y} \right] \sqrt{\det \mathbf{a}_{r1}} \, dx \, dy \\ &\quad + \frac{1}{2} \int_U Y_2 \left[\frac{h_2}{8} \|\mathbf{a}_{r2}^{-1}\mathbf{a}_c - \mathbf{I}\|_{e/Y}^2 + \frac{h_2^3}{24} \|\mathbf{a}_{r2}^{-1}\mathbf{b}_c\|_{e/Y}^2 - \frac{h_2^2}{8} \langle (\mathbf{a}_{r2}^{-1}\mathbf{a}_c - \mathbf{I}), \mathbf{a}_{r2}^{-1}\mathbf{b}_c \rangle_{e/Y} \right] \sqrt{\det \mathbf{a}_{r2}} \, dx \, dy.\end{aligned}$$

and

$$E_{\text{ML}} = \frac{1}{2} \int_U \left[\frac{1}{8} (Y_2 h_2 + Y_1 h_1) \left\| \mathbf{a}_r^{-1} \mathbf{a}_c - \mathbf{I} \right\|_{e/Y}^2 + \frac{1}{24} (Y_2 h_2^3 + Y_1 h_1^3) \left\| \mathbf{a}_r^{-1} (\mathbf{b}_c - \mathbf{b}_r) \right\|_{e/Y}^2 - \frac{1}{8} (Y_2 h_2^2 - Y_1 h_1^2) \left\langle (\mathbf{a}_r^{-1} \mathbf{a}_c - \mathbf{I}), \mathbf{a}_r^{-1} (\mathbf{b}_c - \mathbf{b}_r) \right\rangle_{e/Y} \right] \sqrt{\det \mathbf{a}_r} \, dx \, dy$$

where we defined

$$\begin{aligned} \|\mathbf{A}\|_{e/Y}^2 &= \frac{\nu}{1-\nu^2} \text{Tr}^2(\mathbf{A}) + \frac{1}{1+\nu} \text{Tr}(\mathbf{A}^2) \\ \langle \mathbf{A}, \mathbf{B} \rangle_{e/Y} &= \frac{\nu}{1-\nu^2} \text{Tr}(\mathbf{A}) \text{Tr}(\mathbf{B}) + \frac{1}{1+\nu} \text{Tr}(\mathbf{AB}), \end{aligned}$$

as the elastic energy norm and inner product with the Young's modulus pulled out.

To compute the equivalence relations, we can directly rewrite equations (S1.11), (S1.12) and (S1.13) as

$$\begin{aligned} \frac{Y_1 h_1 \alpha_1^2 + Y_2 h_2 \alpha_2^2}{8} &= \frac{1}{24} (Y_2 h_2^3 + Y_1 h_1^3) + c \\ \frac{Y_2 h_2 \alpha_2 - Y_1 h_1 \alpha_1}{4} &= \frac{1}{8} (Y_2 h_2^2 - Y_1 h_1^2) \\ \frac{Y_1 h_1^2 \alpha_1 + Y_2 h_2^2 \alpha_2}{8} &= \frac{1}{12} (Y_2 h_2^3 + Y_1 h_1^3). \end{aligned}$$

Solving this for α_1 , α_2 , and c gives

$$\begin{aligned} \alpha_1 &= \frac{4h_1^3 Y_1 + 3h_1^2 h_2 Y_1 + h_2^3 Y_2}{6h_1^2 Y_1 + 6h_1 h_2 Y_1} \\ \alpha_2 &= \frac{h_1^3 Y_1 + 3h_1 h_2^2 Y_2 + 4h_2^3 Y_2}{6h_1 h_2 Y_2 + 6h_2^2 Y_2} \\ c &= \frac{(h_1^3 Y_1 + h_2^3 Y_2) (h_1^4 Y_1^2 + 2h_1 h_2 Y_1 Y_2 (2h_1^2 + 3h_1 h_2 + 2h_2^2) + h_2^4 Y_2^2)}{288h_1 h_2 Y_1 Y_2 (h_1 + h_2)^2} \end{aligned}$$

This allows us to write

$$\begin{aligned} \mathbf{a}_{r1} &= \mathbf{a}_r + \left(\frac{4h_1^3 Y_1 + 3h_1^2 h_2 Y_1 + h_2^3 Y_2}{6h_1^2 Y_1 + 6h_1 h_2 Y_1} \right) \mathbf{b}_r \\ \mathbf{a}_{r2} &= \mathbf{a}_r - \left(\frac{h_1^3 Y_1 + 3h_1 h_2^2 Y_2 + 4h_2^3 Y_2}{6h_1 h_2 Y_2 + 6h_2^2 Y_2} \right) \mathbf{b}_r, \end{aligned}$$

and

$$\begin{aligned} \mathbf{a}_r &= \frac{(h_1^4 Y_1^2 + 3h_1^2 h_2^2 Y_1 Y_2 + 4h_1 h_2^3 Y_1 Y_2)}{h_1^4 Y_1^2 + 2h_1 h_2 Y_1 Y_2 (2h_1^2 + 3h_1 h_2 + 2h_2^2) + h_2^4 Y_2^2} \mathbf{a}_{r1} \\ &\quad + \frac{(4h_1^3 h_2 Y_1 Y_2 + 3h_1^2 h_2^2 Y_1 Y_2 + h_2^4 Y_2^2)}{h_1^4 Y_1^2 + 2h_1 h_2 Y_1 Y_2 (2h_1^2 + 3h_1 h_2 + 2h_2^2) + h_2^4 Y_2^2} \mathbf{a}_{r2}, \\ \mathbf{b}_r &= \frac{6h_1 h_2 Y_1 Y_2 (h_1 + h_2)}{h_1^4 Y_1^2 + 2h_1 h_2 Y_1 Y_2 (2h_1^2 + 3h_1 h_2 + 2h_2^2) + h_2^4 Y_2^2} (\mathbf{a}_{r1} - \mathbf{a}_{r2}). \end{aligned} \tag{S1.16}$$

The full energy equivalence then becomes

$$E_{\text{BL}} = E_{\text{ML}} + \int_U \frac{c}{2} \left\| \mathbf{a}_r^{-1} \mathbf{b}_r \right\|_{e/Y}^2 \sqrt{\det \mathbf{a}_r} \, dx \, dy, \tag{S1.17}$$

For equal Young's moduli $Y_1 = Y_2 = Y$ this reduces to equation (S1.14).

S2 Forward problem of growth

This section accompanies the ‘Forward problem of growth’ section of the main text. Here we detail the precise form of the compatibility relations that have to be satisfied for a pair of bilayer metrics, in order for the energetically equivalent curved monolayer to exist. We also show how, following our derivation in the main text, the current result relates to the case of the saddle surface (Fig. 1 in the main text), and the linearized theory for a bimetallic strip [7].

S2.1 Compatibility relations

As mentioned in the main text, when solving the inverse problem we start out with a surface in \mathbb{R}^3 , and so the compatibility equations are satisfied by definition. However, it is an interesting exercise to ask what equations the two layer metrics should satisfy, so that the midsurface of the energetically equivalent monolayer satisfies the compatibility relations. For this, we recall that the equations that describe compatibility for any surface in \mathbb{R}^3 are the Gauss and Peterson-Mainardi-Codazzi equations, which link the entries of first and second fundamental forms [8, 9]. In particular, if the quadratic forms of the grown surface are written as

$$\mathbf{a}_c = \begin{pmatrix} E & F \\ F & G \end{pmatrix}, \quad \mathbf{b}_c = \begin{pmatrix} e & f \\ f & g \end{pmatrix},$$

then the Gauss equation can be written as

$$K = \frac{1}{(EG - F^2)^2} \left\{ \begin{vmatrix} -\frac{1}{2}E_{vv} + F_{uv} - \frac{1}{2}G_{uu} & \frac{1}{2}E_u & F_u - \frac{1}{2}E_v \\ F_v - \frac{1}{2}G_u & E & F \\ \frac{1}{2}G_v & F & G \end{vmatrix} - \begin{vmatrix} 0 & \frac{1}{2}E_v & \frac{1}{2}G_u \\ \frac{1}{2}E_v & E & F \\ \frac{1}{2}G_u & F & G \end{vmatrix} \right\}, \quad (\text{S2.1})$$

which defines the Gauss’ curvature $K = (eg - f^2)/(EG - F^2)$ as an intrinsic property of the surface. The Peterson-Mainardi-Codazzi equations complete the compatibility conditions and are given as

$$\frac{\partial e}{\partial v} - \frac{\partial f}{\partial u} = e\Gamma_{12}^1 + f(\Gamma_{12}^2 - \Gamma_{11}^1) - g\Gamma_{11}^2, \quad (\text{S2.2})$$

$$\frac{\partial f}{\partial v} - \frac{\partial g}{\partial u} = e\Gamma_{22}^1 + f(\Gamma_{22}^2 - \Gamma_{12}^1) - g\Gamma_{12}^2, \quad (\text{S2.3})$$

where the Christoffel symbols are

$$\begin{aligned} \Gamma_{11}^1 &= \frac{GE_u - 2FF_u + FE_v}{2(EG - F^2)}, & \Gamma_{11}^2 &= \frac{2EF_u - EE_v - FE_u}{2(EG - F^2)}, \\ \Gamma_{12}^1 &= \frac{GE_v - FG_u}{2(EG - F^2)}, & \Gamma_{12}^2 &= \frac{EG_u - FE_v}{2(EG - F^2)}, \\ \Gamma_{22}^1 &= \frac{2GF_v - GG_u - FG_v}{2(EG - F^2)}, & \Gamma_{22}^2 &= \frac{EG_v - 2FF_v + FG_u}{2(EG - F^2)}. \end{aligned}$$

The equations (S2.1), (S2.2) and (S2.3) pose three constraints on the surface quadratic forms. In order to translate these constraints to the metrics of the individual layers, let us define the entries of each of the layer metrics as

$$\mathbf{a}_{r1} = \begin{pmatrix} E_1 & F_1 \\ F_1 & G_1 \end{pmatrix}, \quad \mathbf{a}_{r2} = \begin{pmatrix} E_2 & F_2 \\ F_2 & G_2 \end{pmatrix}.$$

Then we can use equation (S1.9) to substitute

$$\mathbf{a}_r = \frac{1}{2} \begin{pmatrix} E_1 + E_2 & F_1 + F_2 \\ F_1 + F_2 & G_1 + G_2 \end{pmatrix},$$

$$\mathbf{b}_r = \frac{3}{4h} \begin{pmatrix} E_1 - E_2 & F_1 - F_2 \\ F_1 - F_2 & G_1 - G_2 \end{pmatrix},$$

into the above compatibility equations (S2.1), (S2.2) and (S2.3). This expresses the compatibility equations in terms of the six entries of the bilayer metrics, and its thickness, instead of the first and second fundamental form of the energetically equivalent monolayer surface.

In summary, equations (S2.1), (S2.2) and (S2.3) provide a way to determine the compatibility of the entries in any given set of bilayer metrics, even in the presence of non-uniform spatial thicknesses, and also in the case of unequal layer thicknesses by using the relations (S1.14) instead of (S1.9). However, the compatibility equations are generally not algebraic, and expose an additional complexity when the thickness h is considered to be an extra, non-uniform degree of freedom. In the remainder of this section, we will discuss some very simple examples, but in general, gaining insight into how these compatibility equations can be interpreted as constraints on the growth mechanism and/or factors will be non-trivial and is left for future work.

S2.2 Specialization for isotropically growing bilayer : spherical surfaces

For a simple application of these equations, consider a bilayer where each layer grows isotropically, so that $\mathbf{a}_{r1} = s_1 \mathbf{I}$ and $\mathbf{a}_{r2} = s_2 \mathbf{I}$, where s_1 and s_2 are allowed to change across the surface. The resulting monolayer surface can then be characterized by

$$\mathbf{a}_c = \frac{s_1 + s_2}{2} \mathbf{I}, \quad (\text{S2.4})$$

$$\mathbf{b}_c = \frac{3(s_1 - s_2)}{4h} \mathbf{I}. \quad (\text{S2.5})$$

We can see immediately that the only non-planar surfaces that can be expressed using these quadratic forms have to be spherical, since the principal curvatures (the eigenvalues of the shape tensor $\mathbf{S} = \mathbf{a}_c^{-1} \mathbf{b}_c$) are equal. However, we can still use it as an example to investigate under what conditions this surface can exist in \mathbb{R}^3 , by examining the Gauss' and Peterson-Mainardi-Codazzi equations. Since the first fundamental form is diagonal, we can use a simplified form of Gauss' equation [9]

$$\frac{eg}{EG} = -\frac{1}{2\sqrt{EG}} \left(\frac{\partial}{\partial u} \frac{G_u}{\sqrt{EG}} + \frac{\partial}{\partial v} \frac{E_v}{\sqrt{EG}} \right). \quad (\text{S2.6})$$

With the current first and second fundamental forms, this gives

$$\frac{9}{4h^2} \left(\frac{s_1 - s_2}{s_2 + s_1} \right)^2 = -\frac{1}{(s_2 + s_1)} \left(\frac{\partial}{\partial u} \frac{(s_2 + s_1)_u}{s_2 + s_1} + \frac{\partial}{\partial v} \frac{(s_2 + s_1)_v}{s_2 + s_1} \right) \quad (\text{S2.7})$$

$$= -\frac{1}{(s_2 + s_1)^3} \left[(s_2 + s_1) ((s_2 + s_1)_{uu} + (s_2 + s_1)_{vv}) - (s_2 + s_1)_u^2 - (s_2 + s_1)_v^2 \right] \quad (\text{S2.8})$$

With uniform non-equal growth factors, this equation can not be satisfied. For non-uniform growth factors, equation (S2.8) provides a second order partial differential equation that the growth factors have to satisfy (point-wise) in order for the strain-free surface to exist.

The Peterson-Mainardi-Codazzi equations simplify as well due to the diagonality of both quadratic forms, and reduce to

$$\frac{\partial e}{\partial v} = \frac{1}{2}E_v \left(\frac{e}{E} + \frac{g}{G} \right), \quad \frac{\partial g}{\partial u} = \frac{1}{2}G_u \left(\frac{e}{E} + \frac{g}{G} \right). \quad (\text{S2.9})$$

Plugging in our assumptions of isotropic growth, we find for the general case where the thickness h is a function of the parametric coordinates (u, v) :

$$\frac{2h(s_1(s_2)_v - s_2(s_1)_v) + h_v(s_1 - s_2)(s_1 + s_2)}{h(s_1 + s_2)} = 0 \quad (\text{S2.10})$$

$$\frac{2h(s_1(s_2)_u - s_2(s_1)_u) + h_u(s_1 - s_2)(s_1 + s_2)}{h(s_1 + s_2)} = 0 \quad (\text{S2.11})$$

This shows that, if one of the growth factors as well as the thickness is homogeneous across the domain, such that for example $(s_1)_u = (s_1)_v = 0$ and $h_u = h_v = 0$, this implies directly that $(s_2)_u = (s_2)_v = 0$, and from the Gauss' equation we can see that the only solution would be $s_1 = s_2$. This means, for isotropic growth of a bilayer where one layer grows uniformly throughout the surface, the only compatible, strain-free (up to embedding-independent strain) solution is a planar scaling of the surface.

Therefore, even for the very simple case of the isotropically growing bilayer, which can only grow into planar or spherical surfaces, it is non-trivial to find compatible bilayer metrics as this involves satisfying three partial differential equations for the growth factors and, possibly, the layer thickness(es).

S2.3 Specialization for orthogonally growing bilayer : saddle surfaces

Figure 1 in the main text concerns the case of linear expansion of each layer in orthogonal directions, so that

$$\mathbf{a}_{r1} = \begin{pmatrix} 1 & 0 \\ 0 & (1+s)^2 \end{pmatrix} \\ \mathbf{a}_{r2} = \begin{pmatrix} (1+s)^2 & 0 \\ 0 & 1 \end{pmatrix},$$

where valid solutions are constrained by $s > -1$. The energetically equivalent monolayer is defined by equation (S1.9) as

$$\mathbf{a}_c = \frac{1 + (1+s)^2}{2} \mathbf{I} \\ \mathbf{b}_c = \frac{3s(s+2)}{4h} \begin{pmatrix} -1 & 0 \\ 0 & 1 \end{pmatrix}.$$

Since neither of the fundamental forms depends on the spatial coordinates, the Peterson-Mainardi-Codazzi equations (S2.9) are automatically satisfied. For the Gauss curvature, we obtain for the left-hand-side of equation (S2.6)

$$K = -\frac{9}{4h^2} \left(\frac{s(s+2)}{s(s+2)+2} \right)^2$$

which is negative for any valid value of s , i.e. whenever $s > -1$. However, the right-hand-side of equation (S2.6) is identically zero, so that Gauss' equation is never satisfied for this particular growth configuration.

S2.4 Specialization for parallel growing bilayer : ‘bimetallic strip’

In this section we specialize the above relations for the case where the two layers grow in parallel directions along the midsurface, but with different growth factors. The linearized approximation of this case was treated almost a century ago [7] to show how a bimetallic strip made of two materials with different coefficients of thermal expansion curves. In that work, it was shown that the curvature of the strip can be written as

$$\kappa = \frac{6(s_2 - s_1) \left(1 + \left(\frac{h_1}{h_2}\right)\right)^2}{(h_1 + h_2) \left(3 \left(1 + \frac{h_1}{h_2}\right)^2 + \left(1 + \frac{h_1 Y_1}{h_2 Y_2}\right) \left(\left(\frac{h_1}{h_2}\right)^2 + \frac{h_2 Y_2}{h_1 Y_1}\right)\right)}, \quad (\text{S2.12})$$

with s_i being the linear growth factors, h_i the thicknesses, and Y_i the Young’s moduli of each layer. Here we will compare our results for a growing bilayer with this equation, for equal as well as unequal layer properties.

In our formulation, assuming that each layer expands linearly by a factor s_i , we can specify the following first fundamental forms of the two layers in their grown rest configurations

$$\begin{aligned} \mathbf{a}_{r1} &= \begin{pmatrix} 1 & 0 \\ 0 & (1 + s_1)^2 \end{pmatrix} \\ \mathbf{a}_{r2} &= \begin{pmatrix} 1 & 0 \\ 0 & (1 + s_2)^2 \end{pmatrix}. \end{aligned}$$

Here we assumed that the initial configuration of each layer is planar and characterized by first fundamental form \mathbf{I} . From the compatibility relations (see previous section), it is easy to see that the corresponding curved configuration is embeddable without conflict, and has zero Gaussian curvature.

In the following we consider the linearized case, assuming small growth factors so that we can approximate $(1 + s_i)^2 \approx 1 + 2s_i$. In this case, for a bilayer with equal thicknesses $h_1 = h_2 = h/2$, we find the following quadratic forms for the energetically equivalent curved monolayer

$$\begin{aligned} \mathbf{a}_r &= \frac{1}{2} (\mathbf{a}_{r1} + \mathbf{a}_{r2}) = \begin{pmatrix} 1 & 0 \\ 0 & (1 + s_1 + s_2) \end{pmatrix} \approx \mathbf{I} \\ \mathbf{b}_r &= \frac{3}{4h} (\mathbf{a}_{r1} - \mathbf{a}_{r2}) = \frac{3}{2h} \begin{pmatrix} 0 & 0 \\ 0 & (s_1 - s_2) \end{pmatrix}, \end{aligned}$$

where in the first relation we neglect terms of $\mathcal{O}(s_i)$ compared to the terms $\mathcal{O}(s_i/h)$ in the second relation. The two principal curvatures, defined as the eigenvalues of the shape tensor $\mathbf{S} = \mathbf{a}_r^{-1} \mathbf{b}_r$, are then equal to the diagonal terms of the second fundamental form \mathbf{b}_r . In this case of equal thicknesses and Young’s moduli, Timoshenko’s theory (S2.12) reduces to

$$\kappa = \frac{3}{2h} (s_2 - s_1),$$

which is exactly what we obtain from our solution for the non-zero principal curvature, up to a minus sign. The minus sign can be explained by noting that, using the definition of principal curvatures as the eigenvalues of the shape operator $\mathbf{S} = \mathbf{a}_r^{-1} \mathbf{b}_r$, the strip normal vectors in [7] point into layer 1, rather than into layer 2 as assumed in this work, so that the definitions of s_1 and s_2 are reversed.

For the case of non-equal layer thicknesses, we can use the relations (S1.14) to find

$$\mathbf{a}_r = \begin{pmatrix} 1 & 0 \\ 0 & 1 + \frac{2s_1h_1^3 + (8s_2 - 2s_1)h_1^2h_2 + (8s_1 - 2s_2)h_2^2h_1 + 2s_2h_2^3}{(h_1 + h_2)^3} \end{pmatrix} \approx \mathbf{I}$$

$$\mathbf{b}_r = \begin{pmatrix} 0 & 0 \\ 0 & \frac{12h_1h_2(s_1 - s_2)}{(h_1 + h_2)^3} \end{pmatrix}$$

where we made the same assumption as above to neglect terms of order $\mathcal{O}(s_i)$ in the first fundamental form. When evaluating this case in Timoshenko's theory, we need to keep in mind that in our energy definition (S1.10), the bottom layer has thickness $h_1/2$ and the top layer has thickness $h_2/2$, whereas in Timoshenko's formula (S2.12) the layer thicknesses are simply h_1 and h_2 . Taking this into account, we obtain from the theory

$$\kappa = \frac{12h_1h_2(s_2 - s_1)}{(h_1 + h_2)^3},$$

which again matches the non-zero principal curvature obtained from our analysis, up to the minus sign as explained above.

Finally, if layer thicknesses and Young's moduli are different, we find from relation (S1.16)

$$\mathbf{a}_r = \begin{pmatrix} 1 & 0 \\ 0 & 1 + \frac{2s_1h_1Y_1(h_1^3Y_1 + h_2^2Y_2(3h_1 + 4h_2)) + 2s_2h_2Y_2(h_1^2Y_1(4h_1 + 3h_2) + h_2^3Y_2)}{h_1^4Y_1^2 + 2h_1h_2Y_1Y_2(2h_1^2 + 3h_1h_2 + 2h_2^2) + h_2^4Y_2^2} \end{pmatrix} \approx \mathbf{I}$$

$$\mathbf{b}_r = \begin{pmatrix} 0 & 0 \\ 0 & \frac{12h_1h_2Y_1Y_2(h_1 + h_2)(s_1 - s_2)}{h_1^4Y_1^2 + 2h_1h_2Y_1Y_2(2h_1^2 + 3h_1h_2 + 2h_2^2) + h_2^4Y_2^2} \end{pmatrix}$$

whereas equation (S2.12) gives, using our definition of h_1 and h_2 as explained above

$$\kappa = \frac{12h_1h_2Y_1Y_2(h_1 + h_2)(s_2 - s_1)}{h_1^4Y_1^2 + 2h_1h_2Y_1Y_2(2h_1^2 + 3h_1h_2 + 2h_2^2) + h_2^4Y_2^2},$$

which is identical to the principal curvature obtained from the second fundamental form.

S3 Inverse problem of growth

This section accompanies the 'Inverse problem of growth' section of the main text, where we show the constraints on the target surface curvatures as a function of the bilayer thickness in order for the energetically equivalent bilayer metrics to be positive definite. Furthermore, we expand on the discussion of the growth trajectory obtained by interpolating initial and target bilayer metrics.

S3.1 Constraint on target surface curvature

Given target shape metrics \mathbf{a}_c and \mathbf{b}_c , the energetically equivalent bilayer metrics are defined as

$$\mathbf{a}_{r1} = \mathbf{a}_c + \frac{2h}{3}\mathbf{b}_c, \quad \mathbf{a}_{r2} = \mathbf{a}_c - \frac{2h}{3}\mathbf{b}_c.$$

For the metrics \mathbf{a}_{r1} and \mathbf{a}_{r2} to be valid metrics, they have to be symmetric positive definite. Their symmetry is guaranteed from the symmetry of \mathbf{a}_c and \mathbf{b}_c . To satisfy positive definiteness, we can equivalently impose that $\mathbf{a}_c^{-1}\mathbf{a}_{r1}$ and $\mathbf{a}_c^{-1}\mathbf{a}_{r2}$ have to have positive eigenvalues, since \mathbf{a}_c is positive definite. This implies that the eigenvalues of $\mathbf{I} \pm (2h/3)\mathbf{S}$, where $\mathbf{S} = \mathbf{a}_c^{-1}\mathbf{b}_c$ is the shape operator, have to be positive. The eigenvalues of \mathbf{S} are the principal curvatures κ_1 and κ_2 of the target surface, and so we find that

$$\max(|\kappa_1|, |\kappa_2|) < \frac{3}{2h}, \quad (\text{S3.1})$$

has to hold for the inverse problem to be solvable. In the case of a bilayer ‘strip’, as discussed in the previous section, if the non-zero principal curvature becomes $3/(2h)$, this implies that one of the growth factors reaches $s_i = -1$, in both the linearized and the non-linear case. This would correspond to a zero-length material element, which is impossible.

Note that based on a spatial self-intersection of the most curved layer in the bilayer, we would expect the condition $|\kappa_i| < 2/h$ for both principal curvatures. Our current constraint of equation (S3.1) is more conservative, implying that self-intersection can never be achieved.

S3.2 Trajectory of growth

The actual process of growth is considered here through interpolation of bilayer metrics, as illustrated in figure S1. Specifically, given an initial surface characterized by fundamental forms $(\mathbf{a}_c^{\text{init}}, \mathbf{b}_c^{\text{init}})$, we can obtain the rest metrics of the bilayer such that the global minimum-energy embedding of its midsurface equals the initial surface (step 1 in the figure). Similarly, we can obtain the rest metrics of the bilayer whose global minimum-energy configuration corresponds to a target surface $(\mathbf{a}_c^{\text{target}}, \mathbf{b}_c^{\text{target}})$ as shown in step 2. Using any possible interpolation scheme we can then obtain the bilayer metrics of intermediate grown states: in the figure we show linear interpolation according to a parameter t , where $0 \leq t \leq 1$ (step 3). Finally, for each of the intermediate, interpolated bilayer metric pair, we can find the corresponding minimum-energy embedding by minimizing the bilayer elastic energy given in equation (S1.4), as shown in step 4 of the figure.

As discussed in the main text, the choice of interpolation scheme can be made depending on the desired characteristics of the interpolated bilayer metrics $(\mathbf{a}_{r1}(t), \mathbf{a}_{r2}(t))$. Linear interpolation ensures positive-definiteness of each intermediate step, whereas log-Euclidean interpolation [10] guarantees moreover monotonically-varying determinants at any point.

In general, however, the intermediate monolayer rest fundamental forms $(\mathbf{a}_r(t), \mathbf{b}_r(t))$ that have an energetic equivalence to the interpolated bilayer metrics $(\mathbf{a}_{r1}(t), \mathbf{a}_{r2}(t))$ are not compatible, so that a strain-free embedding in three-dimensional space does not exist. This issue is similar to that discussed in section S2.1. The question how to interpolate the bilayer metrics so that the energetically equivalent monolayer rest fundamental forms satisfy the compatibility equations, is left for future work.

S4 Results

This section accompanies the ‘Results’ section of the main text. We will first derive inverse-solutions for simple, archetypal geometries of positive and negative Gaussian curvatures. Subsequently, we present details of the numerical method used, and the set-up and results for the flower and face examples presented in the main text.

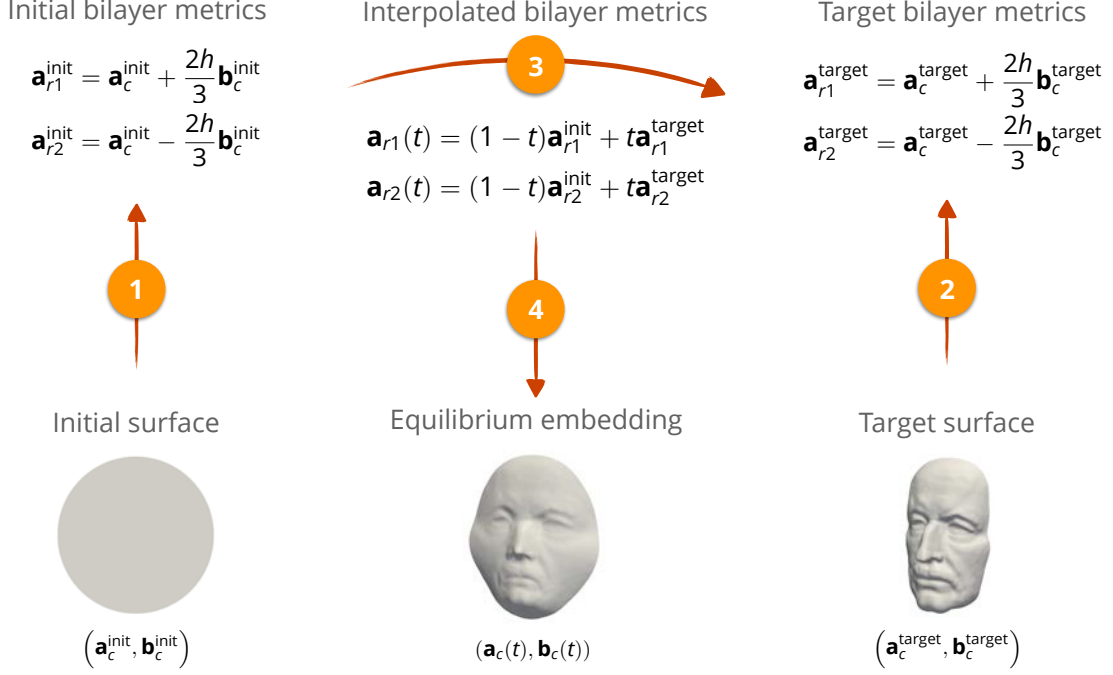


Figure S1: An example of how to grow a disk into a face: by converting the fundamental forms of both the initial surface (1) and the target surface (2) into bilayer metrics, we have specified these two states as global energetic minima corresponding to those metrics. To transition from one state to the other, we can interpolate the two pairs of bilayer metrics, using linear interpolation as shown here (3), or any other interpolation scheme. For each interpolated pair of bilayer metrics, we then compute the corresponding minimum-energy embedding to visualize the growth process (4).

S4.1 Examples for archetypal geometries

Here we show the analytical expressions for \mathbf{a}_{r1} and \mathbf{a}_{r2} for three simple geometric shapes: a hemisphere, catenoid, and saddle. In all these examples, for simplicity, we choose a parametrization so that the original midsurface, prior to growth, is characterized by

$$\vec{m}_r(x, y) = (x, y, 0),$$

so that the corresponding first fundamental form prior to growth is equal to the identity matrix $\mathbf{a}_{r1}^0 = \mathbf{a}_{r2}^0 = \mathbf{I}$. The growth tensor is defined for each layer as

$$\mathbf{a}_{r1} = \delta \mathbf{a}_{r1} \mathbf{a}_{r1}^0 \rightarrow \delta \mathbf{a}_{r1} = \mathbf{a}_{r1} (\mathbf{a}_{r1}^0)^{-1} = \mathbf{a}_{r1},$$

$$\mathbf{a}_{r2} = \delta \mathbf{a}_{r2} \mathbf{a}_{r2}^0 \rightarrow \delta \mathbf{a}_{r2} = \mathbf{a}_{r2} (\mathbf{a}_{r2}^0)^{-1} = \mathbf{a}_{r2},$$

and so we can interpret the final layer metrics as the growth tensors on the initial, ungrown surface.

S4.1.1 Hemisphere

Working with a stereographic projection of a hemisphere with unit radius, growing out of a disk with unit radius, we can write down the parametrization as

$$\vec{m}_c(x, y) = \frac{1}{1 + x^2 + y^2} (2x, 2y, x^2 + y^2 - 1),$$

where $x^2 + y^2 \leq 1$.

The corresponding quadratic forms of the hemisphere are

$$\begin{aligned} \mathbf{a}_c(x, y) &= \frac{4}{(x^2 + y^2 + 1)^2} \mathbf{I} \\ \mathbf{b}_c(x, y) &= \frac{4}{(x^2 + y^2 + 1)^2} \mathbf{I}. \end{aligned}$$

Solving the inverse equations as discussed in the paper provides us with first fundamental forms of a bilayer that will have its energetic equilibrium immersion equal to the hemisphere:

$$\begin{aligned} \mathbf{a}_{r1}(x, y) &= \mathbf{a}_c + \frac{2h}{3} \mathbf{b}_c = \frac{4}{(x^2 + y^2 + 1)^2} \left(1 + \frac{2h}{3} \right) \mathbf{I} \\ \mathbf{a}_{r2}(x, y) &= \mathbf{a}_c - \frac{2h}{3} \mathbf{b}_c = \frac{4}{(x^2 + y^2 + 1)^2} \left(1 - \frac{2h}{3} \right) \mathbf{I}, \end{aligned}$$

which can be interpreted as isotropic inhomogeneous growth of each layer of the original disk.

S4.1.2 Catenoid

For the catenoid, we can work with the following parametrization

$$\vec{m}_c(x, y) = (c \cosh\left(\frac{y}{c}\right) \cos x, c \cosh\left(\frac{y}{c}\right) \sin x),$$

where c is the inner radius of the catenoid. Here $0 \leq x \leq 2\pi$, and $-H/2 \leq y \leq H/2$, where H is the catenoid height. When following this parametrization, we are essentially rolling up a rectangular sheet into a catenoid geometry.

The corresponding quadratic forms of the catenoid are

$$\begin{aligned} \mathbf{a}_c(x, y) &= \cosh^2\left(\frac{y}{c}\right) \begin{pmatrix} c^2 & 0 \\ 0 & 1 \end{pmatrix} \\ \mathbf{b}_c(x, y) &= \begin{pmatrix} c & 0 \\ 0 & -\frac{1}{c} \end{pmatrix}. \end{aligned}$$

Then the bilayer growth that is needed to grow the rectangular sheet into a catenoid is given by

$$\begin{aligned} \mathbf{a}_{r1}(x, y) &= \mathbf{a}_c + \frac{2h}{3} \mathbf{b}_c = \begin{pmatrix} c^2 \cosh^2\left(\frac{y}{c}\right) + \frac{2ch}{3} & 0 \\ 0 & \cosh^2\left(\frac{y}{c}\right) - \frac{2h}{3c} \end{pmatrix} \\ \mathbf{a}_{r2}(x, y) &= \mathbf{a}_c - \frac{2h}{3} \mathbf{b}_c = \begin{pmatrix} c^2 \cosh^2\left(\frac{y}{c}\right) - \frac{2ch}{3} & 0 \\ 0 & \cosh^2\left(\frac{y}{c}\right) + \frac{2h}{3c} \end{pmatrix}, \end{aligned}$$

which can be interpreted as orthotropic inhomogeneous growth of each layer of the original rectangular bilayer. The principal growth directions are the same for each layer, and align with the parameter vectors on the planar sheet.

S4.1.3 Hyperbolic paraboloid

As an example of surface with both positive and negative curvature, we consider growing a hyperbolic paraboloid out of a disk, so that

$$\vec{m}_c(x, y) = (x, y, x^2 - y^2)$$

where $x^2 + y^2 \leq 1$.

This parametrization gives rise to the following quadratic forms

$$\begin{aligned} \mathbf{a}_c(x, y) &= \begin{pmatrix} 1 + 4x^2 & -4xy \\ -4xy & 1 + 4y^2 \end{pmatrix} \\ \mathbf{b}_c(x, y) &= \frac{2}{\sqrt{1 + 4x^2 + 4y^2}} \begin{pmatrix} 1 & 0 \\ 0 & -1 \end{pmatrix}, \\ \mathbf{a}_{r1}(x, y) &= \mathbf{a}_c + \frac{2h}{3} \mathbf{b}_c = \begin{pmatrix} 4x^2 + 1 + \frac{4h}{3\sqrt{4x^2 + 4y^2 + 1}} & -4xy \\ -4xy & 4y^2 + 1 - \frac{4h}{3\sqrt{4x^2 + 4y^2 + 1}} \end{pmatrix} \\ \mathbf{a}_{r2}(x, y) &= \mathbf{a}_c - \frac{2h}{3} \mathbf{b}_c = \begin{pmatrix} 4x^2 + 1 - \frac{4h}{3\sqrt{4x^2 + 4y^2 + 1}} & -4xy \\ -4xy & 4y^2 + 1 + \frac{4h}{3\sqrt{4x^2 + 4y^2 + 1}} \end{pmatrix}, \end{aligned}$$

which can be interpreted as general orthotropic inhomogeneous growth of each layer: performing a spectral decomposition of each matrix reveals the principal growth factors and direction for each of the two layers of the original disk.

S4.2 Numerical method

As shown above, given a mapping $\vec{m} : U \rightarrow \mathbb{R}^3$ that takes any point $(x, y) \in U$ to the three-dimensional embedding of the midsurface, the first and second fundamental forms of the midsurface are, respectively

$$\begin{aligned} \mathbf{a}_c &= \begin{pmatrix} \vec{m}_x \cdot \vec{m}_x & \vec{m}_x \cdot \vec{m}_y \\ \vec{m}_x \cdot \vec{m}_y & \vec{m}_y \cdot \vec{m}_y \end{pmatrix}, \\ \mathbf{b}_c &= - \begin{pmatrix} \vec{m}_x \cdot \vec{n} & \vec{m}_y \cdot \vec{n} \\ \vec{m}_x \cdot \vec{n} & \vec{m}_y \cdot \vec{n} \end{pmatrix}, \end{aligned}$$

where the subscripts x and y denote partial derivatives in those directions, and $\vec{n}(x, y) = \frac{\vec{m}_x(x, y) \times \vec{m}_y(x, y)}{\|\vec{m}_x(x, y) \times \vec{m}_y(x, y)\|}$ is the normal vector to the midsurface.

Using these conventions, we have derived above the bilayer energy of a shell whose midsurface is characterized by quadratic forms \mathbf{a}_c and \mathbf{b}_c , given the layer metrics \mathbf{a}_{r1} and \mathbf{a}_{r2} . Here we will explain how this expression is discretized and implemented for numerical simulations.

In particular, we rely on a triangle discretization of the midsurface, and compute the quadratic forms of each triangle separately in order to evaluate the energy integral. Each triangle is defined by the positions of its three vertices $(\vec{v}_0, \vec{v}_1, \vec{v}_2)$, where $\vec{v}_i \in \mathbb{R}^3$. From this we can compute the edge vectors $\vec{e}_0 = \vec{v}_1 - \vec{v}_0$, $\vec{e}_1 = \vec{v}_2 - \vec{v}_1$, and $\vec{e}_2 = \vec{v}_0 - \vec{v}_2$. Using the edge vectors as tangent vectors to the local plane spanned by the triangle, we can directly compute the first fundamental form of triangle T as

$$\mathbf{a}_T = \begin{pmatrix} \vec{e}_1 \cdot \vec{e}_1 & \vec{e}_1 \cdot \vec{e}_2 \\ \vec{e}_1 \cdot \vec{e}_2 & \vec{e}_2 \cdot \vec{e}_2 \end{pmatrix}$$

For the second fundamental form, we follow [11] and introduce an extra degree of freedom, the unit-length mid-edge normal director defined on each edge of the mesh. In a shear-free setting, as considered here, this director can be defined by a scalar variable, since it is constrained to move in the plane spanned by the normal vectors of two adjacent triangles. The directional derivative of the normal field, as required for the computation of the second fundamental form, is then obtained using a simple difference of the mid-edge normals between two of the three edges of each triangle. In particular, if we denote the edge normal by \vec{n}_i , where $i = 0, 1, 2$ is the edge index, we get the following entries for the discrete second fundamental form:

$$\begin{aligned}(b_T)_{11} &= -\vec{m}_x \cdot \vec{n}_x \approx \vec{e}_1 \cdot 2(\vec{n}_0 - \vec{n}_2), \\ (b_T)_{12} &= (b_T)_{21} = -\vec{m}_x \cdot \vec{n}_y \approx \vec{e}_1 \cdot 2(\vec{n}_1 - \vec{n}_0) = -\vec{e}_1 \cdot 2\vec{n}_0, \\ (b_T)_{22} &= -\vec{m}_y \cdot \vec{n}_y \approx \vec{e}_2 \cdot 2(\vec{n}_1 - \vec{n}_0).\end{aligned}$$

With these discrete quadratic forms, we can evaluate the energy density of the bilayer energy definition for each individual triangle, and sum these over all the triangles in the domain to obtain the total energy. In the context of finite element methods this numerical method is essentially a geometric reformulation of the constant-strain triangle (CST) for the membrane energy, and the Morley triangular element [12] for the bending energy [11, 13].

Once the energy can be computed on a given triangular mesh, we need to find the minimum-energy configuration corresponding to a given combination of $(U, \mathbf{a}_{r1}, \mathbf{a}_{r2})$. For this we perform an iterative, quasi-Newton minimization of the bilayer energy over all vertices and edge director degrees of freedom. The gradients of the discrete energy with respect to the degrees of freedom are implemented algebraically [14].

These operations are implemented using the C++ programming language. We rely on the **Eigen** library [15] for data representations and numerical algebra computations, and the **libigl** library [16] for general operations on the triangle mesh. The energy minimization is performed using an L-BFGS quasi-Newton iterative solver [17].

S4.3 Snapdragon flower

The snapdragon material model was kindly provided by the group of Prof. Coen [18]. We smoothed and remeshed the model to obtain a homogeneous triangle distribution of the surface, resulting in a mesh with 13 500 triangles. The snapdragon mesh was deformed into a cylinder by performing a conformal mapping onto the plane [19, 20], deforming this planar map into a disk, and mapping that disk back up into a cylinder. We set the Poisson ratio of the material to $\nu = 0.3$, and the thickness $0.005R$, where R is the radius of the initial cylinder. We use the log-euclidean approach [10] to interpolate between the metrics, to ensure smoothly varying symmetric positive-definite tensors with monotonically-varying determinants at any point in the growth process.

Directly interpolating between initial and target shapes leads to a meta-stable final state different from the target shape. The reason is the incompatibility between the first and second fundamental form corresponding to the interpolated bilayer metrics, as explained in the main text. Since our numerical process uses the last grown state as initial guess for the next growth step, and since we do not perform a global energy minimization but rather rely on a quasi-Newton algorithm, the final shape is obtained as a local rather than the global energy minimum. In particular, the final shape corresponds to an inversion of the three downward-facing petals, such that they appear on the inside of the flower rather than the outside. Our numerical method does not penalize self-intersection and so the three petals end up intersecting the flower wall (see figure S3, right-most image).

To ensure that the growth process finalizes in the global energy minimum corresponding to the target shape, we create four anchoring states between the initial and final configurations. These intermediate states are computed as a simple linear interpolation of the three-dimensional mesh node positions between the initial and target mesh, and therefore are by construction embeddable in three-dimensional space. For each of these four states, we then computed the first and second fundamental forms, which by extension are compatible. This then allowed us to compute the growth factors required to transition from and to each state according to the method sketched in the main text. This approach breaks the forward problem up into five stages, each of which was simulated by interpolating the growth factors from their initial to their final values, and computing the quasi-static equilibrium configuration for each intermediate growth factor. In total, we used 100 intermediate stages to visualize the growth process.

The difference between these two approaches can be quantified by measuring the monolayer component of the energy corresponding to the bilayer metrics. Recalling the equivalence relation between the energy of bilayers and monolayers described in the main text, we have

$$E_{\text{BL}} = E_{\text{ML}} + \int_U \frac{h^3}{72} \|\mathbf{a}_r^{-1} \mathbf{b}_r\|_e^2 \sqrt{\det \mathbf{a}_r} \, dx \, dy, \quad (\text{S4.1})$$

where

$$\mathbf{a}_r = \frac{1}{2}(\mathbf{a}_{r1} + \mathbf{a}_{r2}), \quad \mathbf{b}_r = \frac{3}{4h}(\mathbf{a}_{r1} - \mathbf{a}_{r2}). \quad (\text{S4.2})$$

If the first and second fundamental forms \mathbf{a}_r and \mathbf{b}_r are compatible, by the Bonnet theory they uniquely describe a surface in three-dimensional space. This surface, characterized by $\mathbf{a}_e = \mathbf{a}_r$ and $\mathbf{b}_e = \mathbf{b}_r$, minimizes the bilayer energy E_{BL} , since the corresponding monolayer component $E_{\text{ML}} = 0$, whereas the second term in the bilayer energy is independent of the embedding. Conversely, if \mathbf{a}_r and \mathbf{b}_r are not compatible, the minimum energy embedding of the bilayer would correspond to a non-zero monolayer energy due to the residual strain in the embedding. We can therefore use the monolayer energy as a measure of the incompatibility between the bilayer metrics, in the context of shell elasticity.

For the direct interpolation, leading to the inverted geometry, the monolayer energy increases almost monotonically during the quasi-static growth process, with a couple of kinks when the geometry snaps between metastable states (see red line in left panel of figure S2). Whereas the starting state (the cylinder) has zero monolayer energy, the final state is characterized by a large monolayer energy, indicating a large residual strain. A visual representation of the monolayer energy density shown in figure S3, indicates that the largest residual strain occurs on the ‘knuckles’ of the three petals, which indeed are curved the wrong way compared to the target shape, resulting in a substantial bending strain.

For the second approach each anchor point corresponds to an embeddable configuration, so that the build-up of residual strain is limited. In between each anchor point the growth process is still characterized by some residual strain, and even at some anchor points a meta-stable state is obtained, but the growth trajectory ultimately leads to the target shape: the residual strain at the final configuration is zero (see red line in right panel of figure S2). As discussed in the main text, more work is required to come up with growth trajectories so that metastable states are avoided, or to control the residual strain in order to achieve different target shapes depending on the spatiotemporal growth pattern.

To measure the error between the final computed shape and the flower target shape we computed the Hausdorff distance, a measure of the maximum distance between the two shapes, which we non-dimensionalize by the square root of the total flower area. This measure is 0.84%, indicating a very close match between the grown shape and the target shape.

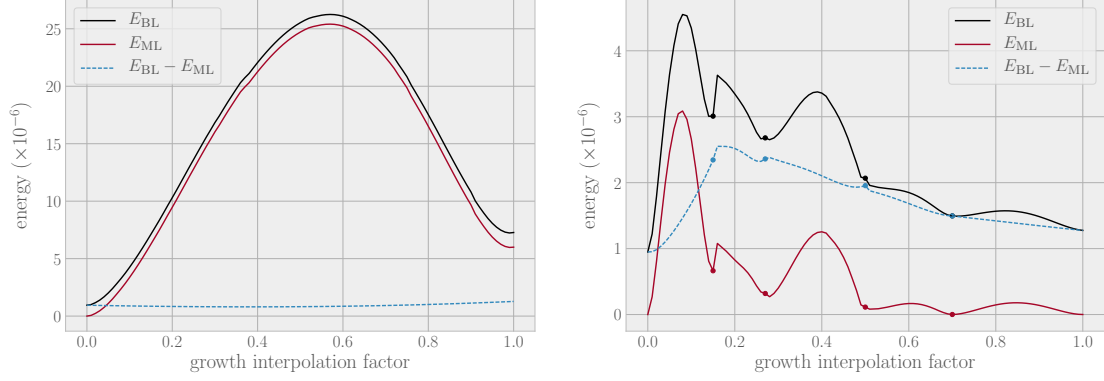


Figure S2: Total bilayer energy (black) decomposed into an embedding-dependent monolayer component (red) and the remaining embedding-independent component (dashed blue). For the case without anchor points (left) the monolayer energy increases significantly, indicating a large build-up of residual strain, including at the final configuration. When we introduce anchor points in the growth process (right, the four anchor points are shown as dots on the lines) the monolayer energy is bounded and the target configuration, characterized by zero monolayer energy, is reached when the growth process is complete. All energies are non-dimensionalized by the Young’s modulus and shell volume.

The natural morphogenesis of the snapdragon flower, which is considered in the main text of this work as an example, has been well-studied [21, 18]. The natural initial state is a cylinder much shorter than the initial configuration used in this work, and furthermore has five small lobes arranged around its upper perimeter. Nevertheless, keeping in mind that this difference amounts roughly to an initial vertical scaling, we can still compare the growth factors and orientations between our results and the natural growth process. Given our results in figure S4, we see remarkable similarities to the biological growth factors described in [21]: the largest growth factors occur at the far end of the lobes, and the directions are mostly consistent, especially on the three downward-oriented petals. We do observe less dominant vertical growth, and more pronounced azimuthal growth on the two large upward-oriented petals, presumably because in our initial tube the corresponding material points are squished together around the perimeter, whereas in the natural initial state they are already separated into lobes. This change between the initial conditions is also likely to reduce or remove the large energetic barrier that has to be overcome in our simulations, which is especially pronounced in the earlier stages of growth.

Follow-up investigations are required to address these differences in more detail, which could be attributed to differences in the initial state, the dynamic adaptation of the growth factors of the natural flower, and the possibility that the natural final configuration has significant deformation-dependent residual strain, as opposed to our solution.

S4.4 Max Planck’s face

The face model was derived from a 3D model of a bust of Max Planck, from which we sliced off the backward half in order to keep only the face, resulting in a mesh with 35 000 triangles. The initial condition was created by conformally mapping the face onto the plane, fixing the boundary vertices along the radius of a disk [19, 20]. The disk was then rescaled to have the same area as the face. We set the Poisson ratio of the material to $\nu = 0.3$, and the thickness

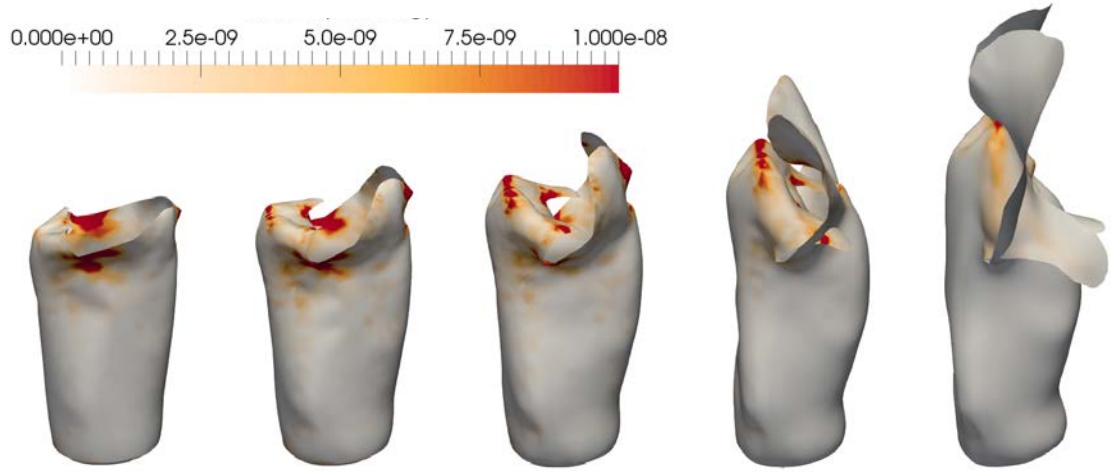


Figure S3: Three-dimensional view of the snapdragon growth without anchor points, at interpolation factors 0.2, 0.4, 0.6, 0.8 and 1.0. The colors denote the distribution of the monolayer energy density E_{ML} over the surface. The final configuration (right) is characterized by inverted petals and, consequently, non-zero monolayer energy.

$0.01R$, where R is the radius of the initial disk. In this case we used 100 intermediate stages created by interpolating the growth factors from their initial to their final values. The total growth of tangent vector lengths on the disk varied between -75% and 300% . The Hausdorff distance between the computed final shape, and the target shape, is 0.91% , where we use the square root of the total face area to non-dimensionalize the metric.

S4.5 Horseshoe bend

Elevation data of the horseshoe bend, a meander of the Colorado river in Arizona, was obtained from the National Elevation Dataset of the U.S. Geological Survey. The horseshoe bend was found in the dataset identified by `n37w112`, with elevation data available in $1/3$ arc-second resolution. The resulting `IMG` file was read using the GDAL library [22], and the pure elevation was extracted. We then sliced the dataset to keep only the horseshoe bend and its immediate surroundings (an area of approximately two by three kilometers, with elevations ranging from 939 m at the bottom of the river, and 1332 m at the top of the canyon), after which the three-dimensional target shape was obtained by warping the elevation data in the direction normal to the plane. The original shape was remeshed using 20 000 triangles, and the planar initial condition was created by conformally mapping the shape onto the plane, while fixing the coordinates of the boundary vertices in the original rectangle shape [19, 20]. We set the Poisson ratio of the material to $\nu = 0.3$, and the thickness $H/131$, where H is the maximum height of the target mesh – compared to the real-life dimensions, this would correspond to a thickness of three meters. Similar to the snapdragon flower, we use anchor points to help guiding the growth trajectory: the first anchor point was created by rescaling the vertical axis of the final configuration by 75% , the second by rescaling the vertical axis by 25% . The total number of intermediate steps used to grow the horseshoe bend is 125. Intermediate metrics were obtained through log-Euclidean interpolation. The Hausdorff distance between the computed final shape, and the target shape, is 0.05% , where we use the square root of the total area to non-dimensionalize the metric.

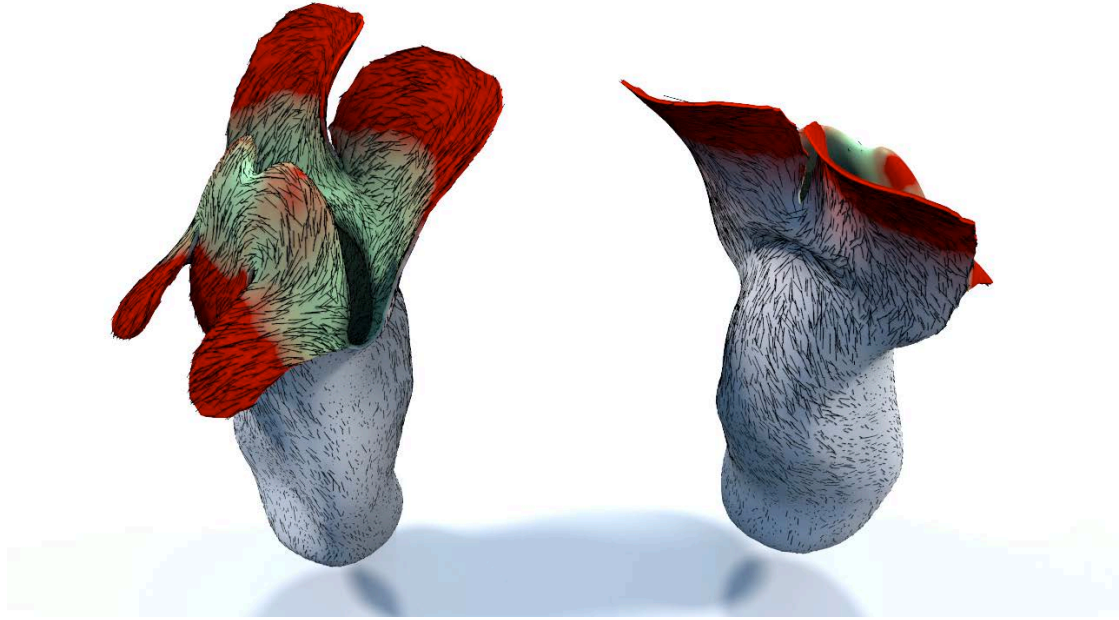


Figure S4: Final grown state of the snapdragon flower with the principal growth orientation (thick black lines) and sum of the two growth factors (colors) overlaid, for the top layer (left) and the bottom layer (right).

References

- [1] E. Efrati, E. Sharon, and R. Kupferman. Elastic theory of unconstrained non-Euclidean plates. *Journal of the Mechanics and Physics of Solids*, 57(4):762–775, 2009.
- [2] C. Weischedel. *A discrete geometric view on shear-deformable shell models*. PhD thesis, 2012.
- [3] B. Audoly and Y. Pomeau. *Elasticity and geometry. From hair curls to the non-linear response of shells*. Oxford University Press, 2010.
- [4] H. Liang and L. Mahadevan. The shape of a long leaf. *Proceedings of the National Academy of Sciences*, 106(52):22049–22054, 12 2009.
- [5] M. Lewicka, L. Mahadevan, and M. R. Pakzad. The Föppl-von Karman equations for plates with incompatible strains. *Proceedings of the Royal Society A: Mathematical, Physical and Engineering Sciences*, 467(2126):402–426, 07 2011.

- [6] M. Lewicka, L. Mahadevan, and M. R. Pakzad. Models for elastic shells with incompatible strains. *Proceedings of the Royal Society A: Mathematical, Physical and Engineering Sciences*, 470(2165):20130604–20130604, 03 2014.
- [7] S. Timoshenko. Analysis of bi-metal thermostats. *Journal of the Optical Society of America*, 11(3):233, 09 1925.
- [8] Manfredo P. do Carmo. *Differential Geometry of Curves and Surfaces*. Prentice-Hall, 1976.
- [9] D. J. Struik. *Lectures on Classical Differential Geometry*. Dover Publications, 2nd edition, 1988.
- [10] V. Arsigny, P. Fillard, X. Pennec, and N. Ayache. Log-Euclidean metrics for fast and simple calculus on diffusion tensors. *Magnetic Resonance in Medicine*, 56(2):411–421, 2006.
- [11] C. Weischedel, A. Tuganov, T. Hermansson, J. Linn, and M. Wardetzky. Construction of discrete shell models by geometric finite differences. Technical Report 220, Fraunhofer ITWM, 2012.
- [12] L. S. D. Morley. The constant-moment plate-bending element. *The Journal of Strain Analysis for Engineering Design*, 6(1):20–24, 01 1971.
- [13] A. Quaglino. A framework for creating low-order shell elements free of membrane locking. *International Journal for Numerical Methods in Engineering*, 108(1):55–75, 03 2016.
- [14] R. Tamstorf and E. Grinspun. Discrete bending forces and their Jacobians. *Graphical Models*, 75(6):362–370, 2013.
- [15] Gaël Guennebaud, Benoît Jacob, et al. Eigen v3. <http://eigen.tuxfamily.org>, 2010.
- [16] A. Jacobson, D. Panozzo, et al. libigl: A simple C++ geometry processing library, 2016. <http://libigl.github.io/libigl/>.
- [17] D. C. Liu and J. Nocedal. On the limited memory BFGS method for large scale optimization. *Mathematical Programming*, 45(1-3):503–528, 08 1989.
- [18] R. Kennaway, E. Coen, A. Green, and A. Bangham. Generation of diverse biological forms through combinatorial interactions between tissue polarity and growth. *PLoS Computational Biology*, 7(6):e1002071, 2011.
- [19] Bruno Lévy, Sylvain Petitjean, Nicolas Ray, and Jérôme Maillot. Least squares conformal maps for automatic texture atlas generation. In *Proceedings of the 29th annual conference on Computer graphics and interactive techniques - SIGGRAPH '02*. Association for Computing Machinery (ACM), 2002.
- [20] P. Mullen, Y. Tong, P. Alliez, and M. Desbrun. Spectral conformal parameterization. *Computer Graphics Forum*, 27(5):1487–1494, 07 2008.
- [21] Amelia A. Green, J. Richard Kennaway, Andrew I. Hanna, J. Andrew Bangham, and Enrico Coen. Genetic control of organ shape and tissue polarity. *PLoS Biology*, 8(11):e1000537, 11 2010.
- [22] GDAL Development Team. *GDAL - Geospatial Data Abstraction Library, Version 2.2.1*. Open Source Geospatial Foundation, 2017.